

Recent Trends in Charged Particle Optics and Surface Physics Instrumentation

Proceedings

15th International Seminar

Skalský dvůr near Brno, Czech Republic

May 29 to June 3, 2016

organized by

Institute of Scientific Instruments The Czech Academy of Sciences

Edited by Filip Mika

Published and distributed by the Institute of Scientific Instruments The Czech Academy of Sciences, v. v. i. technical editing by Miroslav Janáček, printed by MJ servis spol. s.r.o.

Copyright © 2016 by the Institute of Scientific Instruments The Czech Academy of Sciences (ISI CAS) and individual contributors. All rights reserved. No part of this publication may be reproduced, stored in a retrieval system or transmitted in any form or by any means, electronic, mechanical, photocopying, recording or otherwise, without the written permission of the publisher, except as stated below. Single photocopies or single articles may be made for private study or research. Illustrations and short extracts from the text of individual contributions may be copied provided that the source is acknowledged, the permission of the authors is obtained and ISI CAS is notified.

The publishers have made every effort to reproduce the papers at their optimum contrast and with optimum resolution from materials provided by the authors. The publishers accept no liability for the loss of image quality resulting from supply of poor original material or improperly prepared digital records.

ISBN 978-80-87441-17-6

PREFACE

The origins of the seminar “Recent Trends in Charged Particle Optics and Surface Physics Instrumentation” date back into the eighties, when as a part of the isolated “Eastern Bloc”, we were short of English-language books, papers and conferences. The only bright spot was the regular visit of Prof. Tom Mulvey from the University of Aston in Birmingham, who each year spent one month at our Electron Optics Department. It was a great occasion for us to discuss things in English and to learn electron optics and microscopy news from around the world.

In 1989, just before the Iron Curtain fell, we decided to invite more scientists from the West. It was very encouraging for us that all five world-renowned specialists in electron and ion microscopy and lithography accepted our invitation. In September 1989, they met at our Institute at what became the first in a long-standing series of international Seminars. In 1990, at the second Seminar, there were as many as 30 participants from 5 countries. The third Seminar in 1992 was moved to hotel Skalský dvůr in the Bohemian-Moravian Highlands where it has been held as a biannual meeting ever since.

Every two years, we, the organisers, keep asking ourselves the same question: whether we should organise the next Seminar. One cannot overlook one fact about scientific congresses and conferences - there seems to be an increasing number of them, and they take place at very attractive locations. We can't help being a bit apprehensive about whether this trend is going to reflect on our Seminar as well. But when looking at the list of participants, one can be happy at having the opportunity to be here.

The Seminar takes place in a secluded lakeside hotel surrounded by beautiful nature and calm forests, so all participants have a great possibility to see each other every day and to discuss their topics of interest in more detail. This is a great advantage compared to the huge bustling conferences with their many parallel sections, which are a lively celebration of science but sometimes it is difficult to meet there the person with whom you want to discuss a particular scientific topic in more detail.

From the very beginning, the Seminar has been conceived as a meeting devoted more to asking questions not answered yet, than to reporting results. This spirit is usually less present in the introductory presentations and posters but is dominant in the following discussions.

I would like to thank in advance to all who contributed to the 15th Seminar in any respect.

Have an enjoyable and scientifically fruitful stay at the hotel Skalský dvůr.

Iлона Müllerová

CONTENTS

VERY LOW ENERGY STEM / TOF SYSTEM <u>B. Daniel</u> , T. Radlička, J. Piňos, L. Frank and I. Müllerová	6
USING LONGITUDINAL LINEAR FIELD TO IMPROVE THE FOCUSING PROPERTIES OF QUADRUPOLE LENSES IN THE AREA OF FRINGING FIELDS V.S. Gurov, <u>M.V. Dubkov</u> , V.V. Ivanov	8
TREATMENT OF SURFACES WITH SLOW ELECTRONS <u>L. Frank</u> and E. Mikmeková	10
ION COLLECTION SYSTEM FOR SIMS <u>V.S. Gurov</u> , A.A. Trubitsyn, E.Yu. Grachev	12
TOWARDS UNDERSTANDING OF CHARGING EFFECTS OF THIN-FILM PHASE PLATES <u>R. Janzen</u> , J. Schundelmeier, S. Hettler, M. Dries and D. Gerthsen	14
MODELING OF MAGNETIC LENSES FOR SPIN POLARIZATION MANIPULATION <u>M. Johansson</u> and D. Funnemann	16
FURTHER DEVELOPMENTS IN RADIAL MIRROR ENERGY ANALYZER DESIGN W. Han, A. Srinivasan, and <u>A. Khursheed</u>	18
ANNULAR FOCUSED ELECTRON BEAM ABERRATION CORRECTORS <u>A. Khursheed</u> and W. K. Ang	20
FIELD EMISSION FROM THE SURFACE OF HIGHLY ORDERED PYROLYTIC GRAPHITE <u>A. Knápek</u> , Z. Pokorná	22
SEM LEEM – NEW TYPE OF ELECTRON MIRROR MICROSCOPY <u>V. Kolařík</u> , P. Jánský and M. Mynář	24
LARGE-AREA GRAY-SCALE STRUCTURES IN E-BEAM WRITER VERSUS AREA CURRENT HOMOGENEITY AND DEFLECTION UNIFORMITY <u>V. Kolařík</u> , M. Horáček, M. Matějka, S. Krátký and J. Bok	26
BANDPASS FILTER FOR SECONDARY ELECTRONS IN SEM - SIMULATIONS <u>I. Konvalina</u> , F. Mika, S. Krátký and I. Müllerová	28

ELECTRON MANIPULATION WITH LIGHT – ACCELERATION, STREAKING AND FOCUSING OF SUB-RELATIVISTIC ELECTRONS <u>M. Kozák</u> , J. McNeur, N. Schönenberger, A. Li, A. Tafel, and P. Hommelhoff	30
ELECTRON GRATING MIRROR FOR QUANTUM ELECTRON MICROSCOPY <u>M.A.R. Krielaart</u> and P. Kruit	32
NEW DETECTORS FOR LOW-ENERGY BSE <u>O. Lalinský</u> , P. Schauer ¹ , M. Kučera, M. Hanuš, Z. Lučeničová	34
BANDPASS FILTER FOR SECONDARY ELECTRONS IN SEM - EXPERIMENTS <u>F. Mika</u> , I. Konvalina, S. Krátký and I. Müllerová	36
CORRECTION OF THE CHROMATIC AND SPHERICAL ABERRATION IN LOW-VOLTAGE TRANSMISSION ELECTRON MICROSCOPY <u>H. Müller</u> , M. Linck ¹ , P. Hartel, F. Kahl, J. Zach, S. Uhlemann, J. Biskupek, F. Börrnert, Z. Lee, M. Mohn, U. Kaiser and M. Haider	38
SCANNING TRANSMISSION MICROSCOPY AT VERY LOW ENERGIES <u>I. Müllerová</u> , E. Mikmeková, I. Konvalina and L. Frank	40
FABRICATION OF NANO-SLITS FOR A MONOCHROMATOR WITH DOUBLE OFFSET CYLINDRICAL LENSES <u>T. Ogawa</u> , GW. Gang, I.-Y. Park, JH. Kim, S.J. Ahn, and BL. Cho	42
OPTIMAL X-RAY DETECTION FOR THIN SAMPLES IN LOW-ENERGY STEM J. Rozbořil, <u>M. Oral</u> and T. Radlička	44
THE INFORMATION DEPTH OF BACKSCATTERED ELECTRON IMAGING <u>J. Piños</u> , Š. Mikmeková and L. Frank	46
SCANNING VERY LOW ENERGY ELECTRON MICROSCOPY FOR THE CHARACTERIZATION OF POLYCRYSTALLINE METAL SAMPLES <u>Z. Pokorná</u> , A. Knápek	48
CORRECTION OF MISALIGNMENT ABERRATIONS OF A HEXAPOLE CORRECTOR USING THE DIFFERENTIAL ALGEBRA METHOD <u>T. Radlicka</u> , <u>M. Oral</u>	50
DEVELOPMENT OF THE NANO APERTURE ION SOURCE (NAIS) L. van Kouwen, <u>D. Radovanović</u> and P. Kruit	54
DIFFRACTION IN A SCANNING ELECTRON MICROSCOPE <u>T. Řiháček</u> , F. Mika, M. Matějka, S. Krátký and I. Müllerová	56

SECONDARY ELECTRON SPECTROSCOPY AND ENERGY SELECTIVE IMAGING FOR THE ENGINEERING OF CARBON BASED MATERIALS <u>C. Rodenburg</u> , R. Masters, D. Lidzey, M. Uncovsky, T. Vystavel, F. Mika	58
OPTICAL ARRANGEMENTS FOR PHASE-SENSITIVE IMAGING USING ELECTRON PTYCHOGRAPHY <u>J.M. Rodenburg</u> , S.Cao, and A.M. Maiden	60
EFFICIENT LINEAR PHASE CONTRAST AND OPTICAL SECTIONING IN THE ABERRATION-CORRECTED SCANNING TRANSMISSION ELECTRON MICROSCOPE <u>H. Rose</u> and C. Ophus	62
GOLDEN NANOPARTICLE IN OPTICAL TWEEZERS: INFLUENCE OF SHAPE AND ORIENTATION ON OPTICAL TRAPPING <u>M. Siler</u> , O. Brzobohaty, L. Chvatal, V. Karasek, A. Patak, Z. Pokorna, F. Mika and P. Zemanek	64
PRINCIPAL COMPONENT ANALYSIS OF RAMAN SPECTROSCOPY DATA FOR DETERMINATION OF BIOFILM FORMING BACTERIA AND YEASTS <u>M. Siler</u> , O. Samek, S. Bernatova, K. Mlynarikova, J. Jezek, M. Sery, V. Krzyzanek, K. Hrubanova, V. Hola, F. Růžička, P. Zemánek	66
TRAPPING AND COOLING OF SINGLE IONS FOR FREQUENCY METROLOGY AND QUANTUM OPTICS EXPERIMENTS <u>L. Slodička</u> , T.P. Minh, A. Lešundák, V. Hucl, M. Čížek, J. Hrabina, Š. Řeřucha, J. Lazar, P. Obšil, R. Filip, O. Číp	68
A GRAPHENE RING-CATHODE FIELD EMITTER X. Shao, <u>A. Srinivasan</u> , and A. Khurshed	70
A MICROFOCUS X-RAY TUBE WITH HIGH POWER <u>A. Trubitsyn</u> , E. Grachev, M. Dubkov	72
MULTIMODE FIBRES: SEEING THROUGH CHAOS <u>T. Tyc</u> , T. Čížmár and M. Plöschner	74
ELEMENTS OF A GUIDED ELECTRON BASED QUANTUM ELECTRON MICROSCOPE: ELECTRON GUIDE, ELECTRON BEAM SPLITTER AND ELECTRON RESONATOR <u>R. Zimmermann</u> , P. Weber and P. Hommelhoff	76

VERY LOW ENERGY STEM / TOF SYSTEM

B. Daniel*, T. Radlička, J. Piňos, L. Frank and I. Müllerová

Institute of Scientific Instruments of the CAS, v.v.i., Královopolská 147, 61264 Brno, Czech Republic

*e-mail: bdaniel@isibrno.cz

Scanning low energy electron microscopes (SLEEMs) have been built at ISI for over 20 years, either by modification of commercially available SEMs with a cathode lens or completely self-built in case of a dedicated ultra-high vacuum scanning low energy electron microscope (UHV SLEEM) [1]. Recently, the range of detection methods has been extended by a detector for electrons transmitted through ultrathin films and 2D crystals like graphene [2]. For a better understanding of interaction between low energy electrons and solids in general, and the image contrast mechanism in particular, it was considered useful to measure the energy of transmitted electrons. This allows a better comparison with simulations, which suffer from increasing complexity due to a stronger interaction of electrons with the density of states at low energies.

The energy analysis will be done by time-of-flight (TOF) measurements in an UHV SLEEM (drawing of the setup in Fig. 1) with a primary electron beam energy of 5 keV and a cathode lens assembly for beam deceleration to arbitrarily low landing energies. Multiple detectors will be integrated in the system, similar to the aforementioned existing UHV SLEEM [2]: a disk-shaped YAG scintillator with 300 micron coaxial bore for detection of off-axis backscattered electrons, a MEDIPIX position sensitive detector intended for electrons escaping through the scintillator's central bore with possible deflection of this flux to an integral scintillator detector, and a retractable scintillator detector for total current of transmitted electrons to be used interchangeably with another MEDIPIX detector for acquisition of the angular distribution of the transmitted electrons and with the TOF spectrometer.

The TOF system visible in the lower part of Fig. 1 consists of a 700 mm drift tube with a focusing lens to increase the acceptance angle up to 20° and an electron detector. The detector itself has a mesh in front of it to prevent its bias voltage from altering the electric field in the drift tube. It is a commercially available assembly by RoentDek that consists of an MCP stack with 40 mm active diameter and a metal plate anode with corresponding mounting. A time-to-digital converter (TDC) and other necessary electronics for data acquisition will also be provided by RoentDek. While the TDC has the drawback of about 10 ns dead time when compared to an ADC, data acquisition and analysis is much simpler. With an expectation of less than one electron per pulse, dead time will only rarely lead to loss of signal.

Pulsing will be done by beam deflection using the centering deflector in the condenser of the electron gun. When centered, the beam passes through a narrow slit, otherwise it is blocked. While with this method the pulse duration is nowhere near pulsed laser triggered photoemission sources, pulses of 1 ns length are expected. This range is similar to the time resolution expected from the detector, and similar to the time of flight spread due to variation

of possible flight lengths of deflected electrons collected by the focusing lens. For achieving the desired resolution of at least 1 eV, the TOF analyser will be mostly used with very low energy electrons below 50 eV. At even lower energies the resolution is improved, but still limited by the source spread of 0.5 eV.

The device is projected as a completely bakeable UHV one with expected working pressure in the order of 10^{-10} mbar. At present the vacuum chambers are being assembled and tested, the electron column is already in operation in a testing apparatus and the setup of detectors is partly ready for installation and partly designed and by stages manufactured. [3].

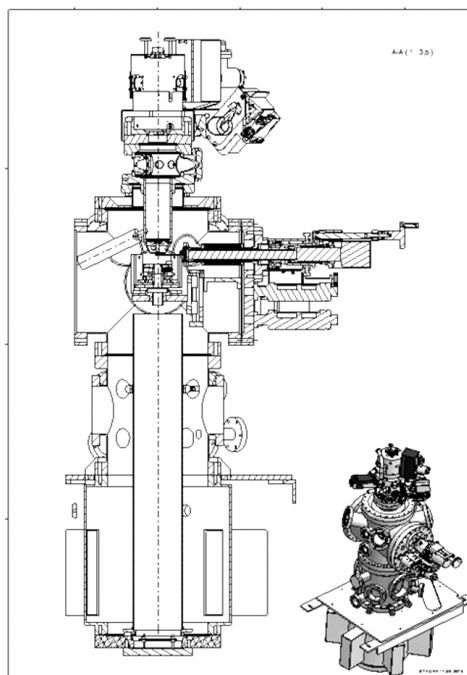


Figure 1 Drawing of the UHV setup with 3D view in the bottom right corner.

References:

- [1] Müllerová I. and Frank L., *Adv. Imaging Electron Phys.* **128** (2003), p. 309-443.
- [2] Müllerová I., Hovorka M., Hanzlíková R. and Frank L., *Material Transactions* **51** (2010), p. 265-270.
- [3] The research was supported by SIMDALEE2 (Marie Curie FP7-PEOPLE-2013-ITN Grant # 606988) and CAS (RVO:68081731).

USING LONGITUDINAL LINEAR FIELD TO IMPROVE THE FOCUSING PROPERTIES OF QUADRUPOLE LENSES IN THE AREA OF FRINGING FIELDS

V.S. Gurov, M.V. Dubkov, V.V. Ivanov

Ion-optical systems on the basis of quadrupole lenses possess mapping properties. Independently on a value of initial phases of ion input to the radio-frequency field of such lens through the time equal to a half-period of secular oscillations of these ions, their coordinates and velocities in the plane perpendicular to the system longitudinal axis (z -axis) are repeated up to sign. For ions with chosen mass-to-charge ratio it is possible to ensure a half-period multiplicity of their secular oscillations at transverse coordinates x and y by setting parameters of radio-frequency voltage under known system geometrical dimensions. It is possible to carry out an accurate transfer of ions from input to output of the electrode system (analyzer) by matching selected ion transmit time through the quadrupole lens with a period of their secular oscillations. It allows receiving the transmission of ion flows close to 100% and controlled ion velocity spread in the transverse direction at output of an analyzer. The latest fact is significant because it allows effectively using an output flow of ions in future: for example, in tandem mass-spectrometry. Selectivity of ions at the output relative to mass-to-charge can be provided by inputting the ion flow at the angle to the longitudinal axis of an analyzer. Besides, ions with other mass-to-charge value than the selected ones will be sorted out both at the expense of large values of ions secular periods of oscillations at transverse x - or y -coordinates and at the expense of greater amplitudes of oscillations at this coordinate.

One of the main issues of the described method is a presence of fringing fields in the system. The analysis has shown that input fringing field is a reason of significant growth of oscillation amplitudes at the transverse coordinate. Output area deteriorates a field in the area of ion flow output by decreasing a transmission coefficient and increasing ion velocity spread in the transverse direction.

For this issue solution, we suggest to form a longitudinal (along z -axis) uniform electrical field in the area of fringing fields along with a quadrupole transverse field. Such field can be described by the following relation:

$$\varphi(x, y, z) = b_x x^2 + b_y y^2 + cz, \quad (1)$$

where b_x , b_y , c – coefficients determined at the level of Laplace's equation and boundary conditions.

Result of the relation (1) analysis is a system of equations describing surfaces of the electrode system named as a quadrupole cell with longitudinal field:

$$\begin{cases} \frac{y^2 - x^2}{y_a^2} = 1 + \frac{z}{l} (K_0^2 - 1) \\ \frac{y^2 - x^2}{y_a^2} = \frac{z}{l} (K_0^2 - 1) \end{cases}, \quad (2)$$

where l – a length of such cell, $K_0 = \frac{y_{al}}{y_a}$, $y_a y_a$ and $y_{al} y_{al}$ – characteristic analyzer dimensions under $z = 0$ $z = 0$ and $z = l$ correspondingly.

On basis of the electrode system described by relation (2), separate modular constructions can be formed for input of ion flows into quadrupole lenses and output from them (fig. 1). Such system has a range of advantages. Firstly, it increases a quality of the fringing field retaining a distribution square-law characteristic of its potential in the analyzer transverse direction. It allows realizing one more of the quadrupole lens advantages – independence of ion motion along x -, y - and z - coordinates. And secondly, such system allows determining a fringing field length by choosing a coefficient value K_0 decreasing its negative influence.

Results of the executed comparative numerical simulation have shown that application of the suggested system allows twice decreasing a length of the fringing fields and more in comparison with a fringing field formed under presence of plane diaphragms that leads to a significant decrease of ion loss caused by uncontrolled growth of their oscillation amplitude at the transverse coordinate in the present field.

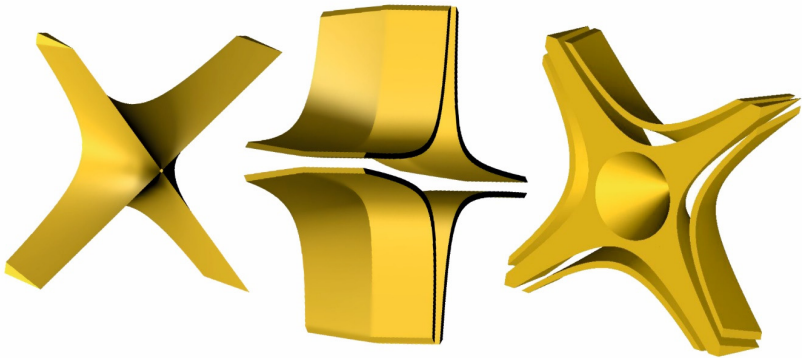


Figure 1

TREATMENT OF SURFACES WITH SLOW ELECTRONS

L. Frank* and E. Mikmeková

Institute of Scientific Instruments of the CAS, Královopolská 147, 61264 Brno, Czech Republic

*e-mail: ludek@isibrno.cz

Historically, the most annoying obstacle to acquiring SEM micrographs, in particular higher magnification micrographs taken with the ambition of resolving the finest observable details, may be said to be carbonaceous contamination “highlighting” the previous field of view with a black rectangle contoured by an even darker frame. This contamination is generated by decomposition of adsorbed hydrocarbon molecules with incident electrons leaving a cross-linked layer of carbon atoms as a surface coating. The darker contours come from high surface mobility of hydrocarbon molecules from outside the field [1]. The situation has been improved in recent decades by a lower pressure and dryer vacuum in specimen chambers, but even under ultrahigh vacuum (UHV) conditions the phenomenon occurs due to hydrocarbon molecules deposited on the specimen when loaded. Therefore, only in-situ cleaning with an attachment producing an ion beam solves this problem in UHV, while some plasma cleaners have also started appearing in standard-vacuum SEM chambers. The goal of complete removal of hydrocarbons is motivated by the supposed unavailability of their decomposition with primary electrons. However, we have found hydrocarbon molecules being released, rather than their decomposition, when the energy of the impinging electrons drops beneath 50 eV or so.

The removal of the adsorbed molecules is a kind of radiation damage that has to be stopped before the sample itself is affected, but monitoring of this phase requires imaging the surface at a low energy of electrons. This is available in a SEM [2] or even STEM [3] equipped with a cathode lens. We have chosen single-layer graphene observed in the STEM mode as an optimum specimen for these experiments. Removal of adsorbents is demonstrated by progressively increased transmissivity of slow electrons accompanied by their decreasing reflectivity (Fig. 1). The possibilities for undesirable damage of an already cleaned sample are restricted here only to perforation of the sample (Fig. 2) that cannot be overlooked.

We have carefully examined the dependence of the phenomenon on the energy of the bombarding/imaging electrons and their dose and current. While under UHV conditions the cleaning effect is simply enhanced when decreasing the electron energy, under standard vacuum conditions we observe contaminated frames the darkness of which intensifies down to around 200 eV. Below this threshold the contamination weakens, and below around 100 eV it switches to removal of the transmissivity reducing layers (Fig. 2) [4] provided the sample has been heated before loading. The cleaning effect culminates at around 50 eV, though it is preserved down to tens of eV. In addition to the dose dependence, at certain energies of incident electrons some effects are also observed in dependence on the beam current, specimen bias, etc. (Fig. 3).

The possibility of removing the hydrocarbon molecules in-situ even under standard vacuum conditions may pave the way to the performance of some surface-sensitive studies under less strictly limited vacuum conditions [5].

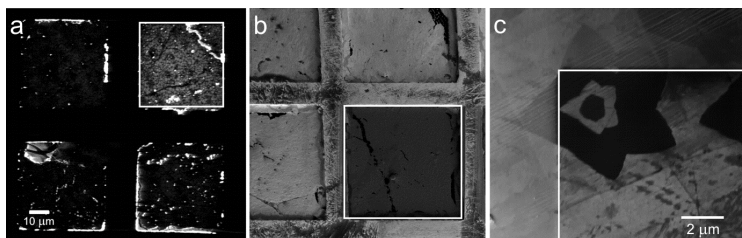


Figure 1 Prolonged exposition of marked areas with 30 eV electrons: image in transmitted (a) and reflected (b) electrons at 30 eV of suspended graphene on lacey carbon, reflected electron image at 3 eV of CVD graphene on Cu (c).

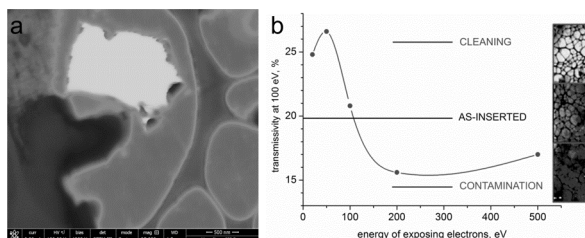


Figure 2 Hole drilled into graphene with 0.8 nA of 500 eV electrons in a dose of 10 Ccm⁻² (a), energy dependence of the influence of electron impact on suspended graphene (b).

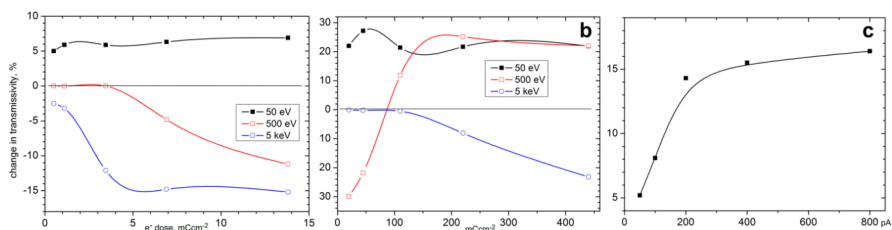


Figure 3 Changes in transmissivity of suspended graphene for 100 eV electrons induced by 25 pA (a) and 0.8 nA (b) incident currents, and by 15 mCcm⁻² dose of 50 eV electrons delivered by various currents (c).

References:

- [1] Reimer L., Scanning electron microscopy, Springer 1998, Sect. 3.5.4.
- [2] Müllerová I. and Frank L., Adv. in Imaging and Electron Phys. **128** (2003), p. 309-443.
- [3] Müllerová I., Hovorka M. and Frank L., Ultramicroscopy **119** (2012), p. 78-81.
- [4] Mikmeková E., Frank L., Müllerová I., Li B.W., Ruoff R.S. and Lejeune M., Diamond & Rel. Mater. **63** (2016), p. 136-142.
- [5] The research was supported by TACR (TE01020118) and MEYS CR (LO1212), its infrastructure by EC (CZ.1.05/2.1.00/01.0017) and CAS (RVO:68081731).

ION COLLECTION SYSTEM FOR SIMS

V.S. Gurov*, A.A. Trubitsyn, E.Yu. Grachev

Ryazan State Radio Engineering University, 390005 Ryazan, Gagarina st. 59/1

*e-mail: gurovvs@mail.ru

Acquisition of high analytical characteristics of devices for the substance analysis by SIMS methods is only possible under optimal matching of a charged particle source and mass spectrometer analyzer. Mass-analyzers of the time-of-flight type and quadrupole systems applied in SIMS require monoenergetic and weakly diverging ion fluxes at the input to support normal operation. So a system of the ion flux formation should provide:

- collection of charged particles from the large solid angle;
- selection of charged particles according to energies;
- optimal focusing of charged particles on input of the used mass-analyzer;
- optical isolation of areas where secondary ions are formed and their registration to improve a signal-to-noise ratio.

Various systems such as simple diaphragms and systems of the “spherical diode” type and devices including known types of energy-analyzers are used to succeed in stated objectives [1]. However, mentioned systems have a low coefficient of the particle collection, low quality of the energy selection, complicated acquisition of a weakly diverging cylindric flux of charged particles at the output for their optimal injection into the mass spectrometer analyzer.

Two-stage systems suggested by authors of the paper are more effective for the ion flux formation. Such systems use axisymmetric cone and hyperbolic electrodes. The first system stage forms specified energetic parameters of the charged particle flux and the second one ensures an acquisition of required geometrical characteristics.

Calculation of the first stage parameters has been carried out primarily for calculation of suggested systems: geometry factor, distance to a source, energy factor, width of the output selection slit. Obtained results have been used for calculation of the second stage by numerical methods.

Authors have carried out a calculation and design of the two-stage system containing the following basic units: input conical system, first lens composed of a ring hyperbolic electrode and two end cone electrodes, second lens composed of a ring hyperbolic electrode and two end hyperbolic electrodes. The whole system is installed into the electrostatic screen.

Suggested system of the ion flux formation has the following design parameters:

- ion collection coefficient – 4 %;
- resolution capability according to energies – 15 at the level 0.5;
- diameter of the output ion flux – $0,2r_a$, where r_a – an internal radius of the lens ring electrode,
- angular flux divergence – 10° ,
- diameter of the collection system – not more than 90 mm,

- distance from the system input to the ion source – not more than 20 mm,
- ratio of the ion energy to the first lens ring electrode potential (coupling coefficient) – 1.4

Design represented in Fig.1 has been constructed for the experimental evaluation of formation system parameters. Dimensions of the whole device do not exceed 62×84 mm.



Figure 1 Image of the collection system.

Experimentally found values of the resolution capability and coupling coefficient have been equal to $R_{0,5}=15$ and $k_{ce}=1,39$ that corresponds to calculated values. Comparison of the energy peak design form with experimentally obtained one has shown its good qualitative coincidence.

References:

[1] Victor S. Gurov, Arman O. Saulebekov, Andrey A. Trubitsyn. Analytical, Approximate-Analytical and Numerical Methods in the Design of Energy Analyzers. In P.W. Hawkes (Ed.), Advances in Imaging and Electron Physics: Vol. 192. – 2015.- London: Academic Press, 209 p.

TOWARDS UNDERSTANDING OF CHARGING EFFECTS OF THIN-FILM PHASE PLATES

R. Janzen^{1*}, J. Schundelmeier¹, S. Hettler¹, M. Dries¹ and D. Gerthsen¹

¹Laboratory for Electron Microscopy, KIT, Engesserstraße 7, 76131 Karlsruhe, Germany
*e-mail: info@dr-janzen.de

In the past few years, physical phase plates (PP) have become a viable tool to enhance the contrast of weak-phase objects in transmission electron microscopy (TEM). Here we focus on thin-film PPs where the mean inner potential is exploited to impose a phase shift on electrons propagating through the PP [1]. The application of thin-film PPs is hampered by deviations of the phase shift from its desired value which occur due to charging of the thin film. Our experimental approach to overcome charging of thin-film PPs was using the metallic glass alloy Pd77.5Cu6.0Si16.5 (PCS) with a high specific conductivity of $1.18 \cdot 10^6$ S/m [2] as PP material. However, Hilbert PPs fabricated from thin PCS films nevertheless show pronounced distortions of the Thon-ring system during illumination with 200 keV electrons. These observations initiated the development of a theoretical model to obtain an improved understanding of charging, which is presented in this work.

Charging is described by assuming a charge-dipole layer to be present at the PP. A possible source for such a dipole layer could be an insulating contamination layer on top of the PCS film in the illuminated PP region which could capture and fix low-energy secondary electrons generated by the primary electrons in the PCS film. Together with its positive mirror charge in the grounded electrically conducting PCS film this fixed charge would form a dipole layer. The dipole strength is assumed to be proportional to the current density distribution in the back focal plane which can be qualitatively obtained from a diffraction pattern. The proportionality factor for the dipole strength is a fit parameter denoted as phase mask amplitude in the following.

As a test of our model we compare power spectra obtained from an experimental image of an amorphous carbon (aC) thin-film test object with a simulation based on our model. The experimental reference image was obtained by using a PCS film-based Hilbert PP installed in the back focal plane of a Philips CM 200 FEG/ST transmission electron microscope. In the simulation we assume the Hilbert PP to be illuminated by the current density distribution given by the diffraction pattern and calculate the phase shift in the back focal plane. The resulting dipole strength distribution is then fed into an image simulation procedure which yields simulated power spectra as a function of the phase mask amplitude. The latter is optimized by a comparison with the experimental reference. The experimental reference and calculated power spectra are compared pixel by pixel. The sum of all pixel comparisons belonging to one pair of power spectra serves as measure of agreement, which is plotted for different phase mask amplitudes in Figure 1 for the region below the cut-on frequency. Best agreement of almost 75% is obtained. This is remarkable taking into account that experimental and simulated spectra (based on noisy input for the illumination data) contain noise.

Figure 2 shows a montage of a simulated and experimental power spectrum. Two regions, below and above the cut-on frequency, can be distinguished in the power spectra. The cut-on frequency is given by the distance between the PP edge and the zero-order beam and is marked by vertical white lines. Note the good agreement between experimental and simulated spectra, especially below the cut-on frequency.

Overall our method seems to be a promising approach to analyze and explain phase shift distortions due to charging in thin-film PP applications.

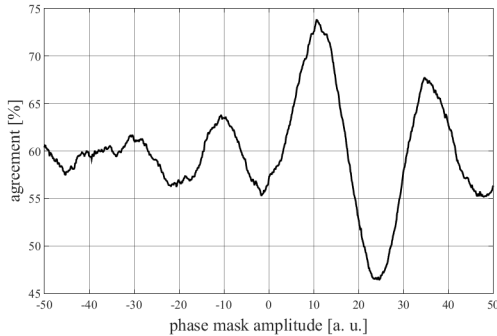


Figure 1 Agreement between experimental and simulated power spectra for spatial frequencies below the cut-on frequency as a function of the fit parameter (phase mask amplitude). Best agreement of almost 75% is obtained. This is remarkable taking into account that experimental and simulated spectra (based on noisy input for the illumination data) contain noise.

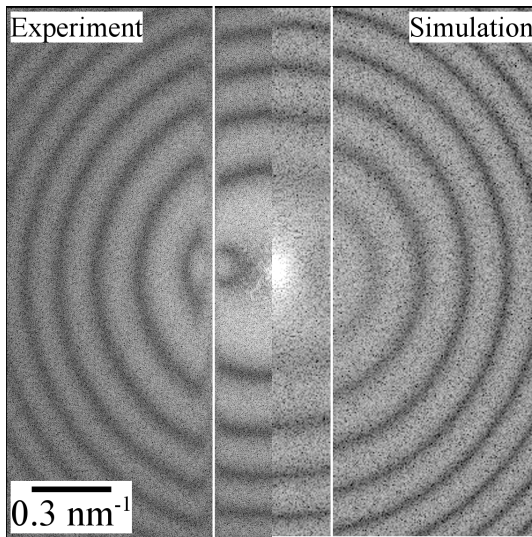


Figure 2 Montage of an experimental power spectrum of an aC test object and a simulated power spectrum. The white lines mark the cut-on frequency of the Hilbert PP which is determined by the distance between the zero-order beam and the edge of the PP. The complementary behavior of the Thon-rings below and above the cut-on frequency demonstrates the desired phase-shifting properties of the Hilbert PP.

References:

- [1] R. Danev and K. Nagayama, *J. Phys. Soc. Jpn.* 73 (2004), p. 2718.
- [2] B. Chelluri and R. Kirchheim, *J. Non-cryst. Solids* 54 (1983), p. 107.
- [3] Financial support by the Deutsche Forschungsgemeinschaft (DFG).

MODELING OF MAGNETIC LENSES FOR SPIN POLARIZATION MANIPULATION

M. Johansson^{1*} and D. Funnemann¹

¹SPECS Surface Nano Analysis GmbH, Voltastrasse 5, 13355, Berlin, Germany

*e-mail: Martin.Johansson@specs.com

Magnetic fields are commonly used to manipulate the spin polarization vector [1,2]. Under the assumption of a homogeneous, axial magnetic field, it follows that

$$\eta = g^* \varphi \quad \text{Eq. 1}$$

, where η is the angle of rotation of the spin polarization vector around the optical axis, φ the rotation angle of the electron optical image around the optical axis and g the gyromagnetic ratio, $g = 2.00232$ [3,4].

In practice, it is difficult to produce a spatially limited homogeneous magnetic field with high accuracy. However, simulations of the precession of the spin polarization vector along the electron trajectories, as well as experimental evidence, suggest that Eq. (1) holds also for the non-homogeneous magnetic field generated in a standard magnetic electron optical lens. This opens up the possibility of minimizing the imaging errors of the optical system, while using Eq. 1 to determine η . This principle was used in the design of the SPECS 3D-Spin detectors, where a magnetic lens in combination with a 90° electrostatic deflector is used to select which of the polarization vector components is analyzed (patent PCT/EP2011/070226). Fig. 1 shows the principles of the 3D- Spin Detector and Fig. 2 the magnetic field on the optical axis of the Spin Rotation Lens along with η and φ .

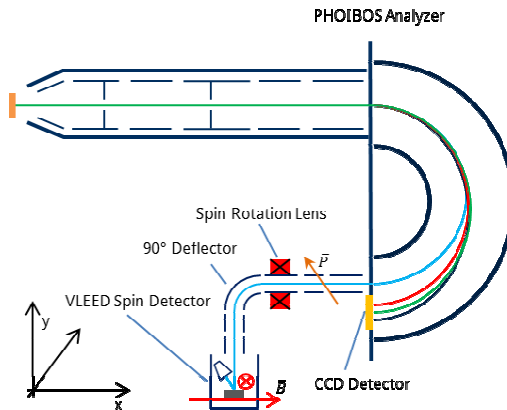


Figure 1 Principles of the SPECS 3D-Spin detector mounted on a SPECS PHOIBOS electron spectrometer.

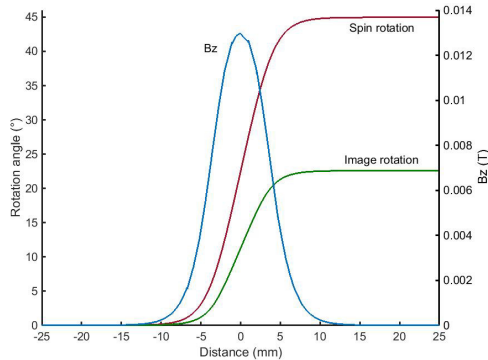


Figure 2 The magnetic field on the optical axis, B_z , the image rotation angle, φ , and the spin rotation angle, η , for the SPECS spin rotation lens.

From Eq. 1, variations in φ over an electron optical image is expected to result in corresponding errors in η . From the calculations made so far, it seems that the deviations in η are smaller than in φ . Fig. 3 shows calculated values for η over a representative ensemble of electrons at the VLEED Spin detector (see Fig. 1). The deviation in η from the desired value of 45° is below $\pm 0.25^\circ$. The deviations are partially due to the numerical accuracy of the simulation.

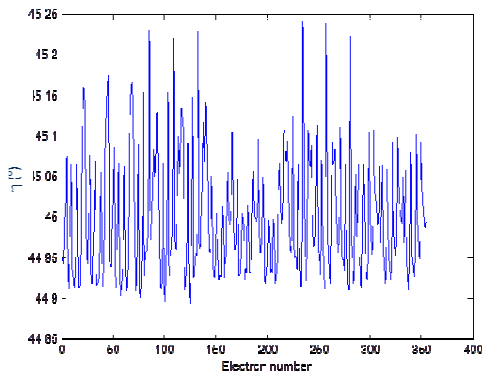


Figure 3 The calculated spin rotation angle, η , for a representative electron ensemble.

The experimental results obtained with the SPECS 3D-Spin detector so far confirm the assumption that Eq. 1 holds generally. However, we have not been able to find a proof of Eq. 1 for a non-homogeneous magnetic field in the literature.

References:

- [1] Duden T., Bauer E., Rev. Sci. Instrum. **66** (1995), p. 2861.
- [2] Engwall D.A., Dunham B., M., Nucl. Instr. Meth. **A324** (1993), p. 409-420.
- [3] Bargmann V., Michel L., Telegdi V. L., Phys. Rev. Lett. **2** (1959), p. 435.
- [4] W. Glaser, Grundlagen der Elektronenoptik (Springer, Wien, 1952).

FURTHER DEVELOPMENTS IN RADIAL MIRROR ENERGY ANALYZER DESIGN

W. Han, A. Srinivasan, and A. Khurshed*

Department of Electrical and Computer Engineering, National University of Singapore, Singapore 117576

*e-mail: eleka@nus.edu.sg

This paper will report some recent developments of two radial mirror energy analyzers that were designed as add-on attachments for focused electron beam instruments, the wide-band multi-channel Parallel Radial Mirror Analyzer (PRMA) [1], and the sequential Radial Mirror analyzer (RMA) [2]. Both these analyzer designs combine second-order focusing properties with 2π detection, and are predicted to have significant energy resolution-transmittance advantages over previous energy analyzer designs.

Further experiments on a PRMA prototype attachment inside a Scanning Electron Microscope (SEM) were carried out, as shown in Fig. 1a, beyond the preliminary results reported so far [3]. They indicate that correct alignment of the primary beam to the analyzer's axis of symmetry is important. Significant improvement in the shape of experimental secondary electron (SE) analyzer signals were obtained when the position of the primary on the specimen was varied. The PRMA was run in sequential mode with a single detector, and at first, the SE analyzer signals appeared much broader than expected. However, by varying the position of the primary beam on the specimen, SE analyzer signals very similar to those previously obtained by a second-order focusing toroidal energy analyzer were obtained where negative voltages were applied to the specimen [4]. These results are shown in Fig. 1b. A simulation study using Lorentz 3EM was also performed, showing that a misalignment of 0.5 mm along the direction perpendicular to the symmetry plane degraded the resolution by a factor of 2.24.

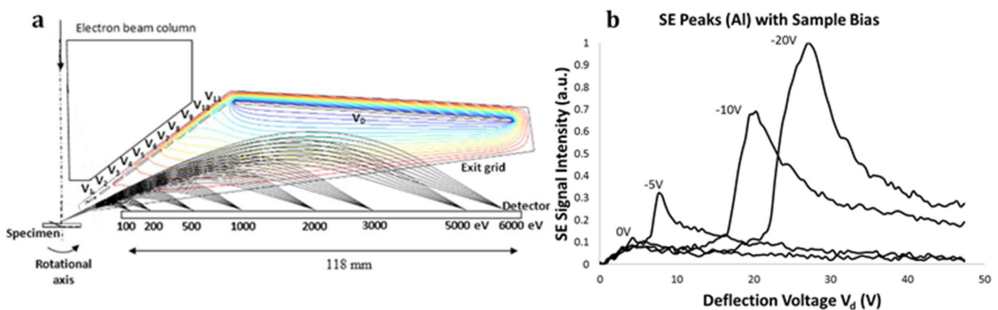


Figure 1 (a) Schematic of the experimental setup. (b) Experimental SE Spectra measured at different specimen bias voltages.

For the RMA design, the effect of a non-ideal entrance grid on the analyzer's predicted energy resolution was simulated. A simple grid model was used (Figure 2) consisting of metal radial wires that appear to radiate out from the rotationally symmetric axis of the analyzer. Direct ray tracing was carried using the 3D version of Lorentz program [4]. Fringe electric fields in the space between the grid radial wires were found to both cause a shift in the focal point in the detection plane and enlarge its size. The simulated relative energy resolution was calculated as a function of grid transparency and is given in Table 1 for the entrance polar angular range of $\pm 6^\circ$. A 50% grid transparency is predicted to degrade the relative energy resolution by a factor of around 2.5 (0.038%).

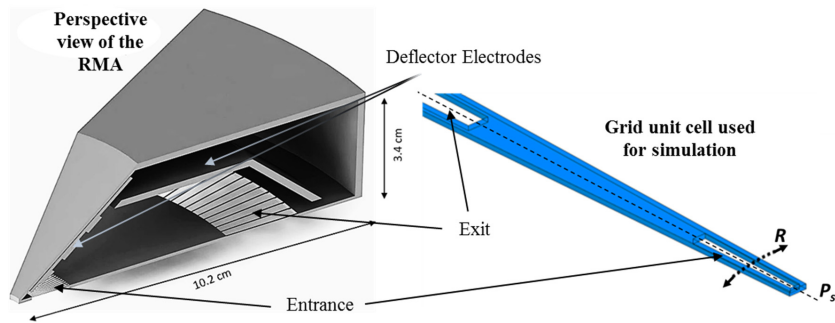


Figure 2 Simulation of analyzer entrance/exit radial wire grids: (a) Three dimensional perspective view of the RMA and simulation grid unit cell model.

Transparency (%)	Average Simulated % energy relative resolution for pass energy E_p
0	0.015
25	0.027
37.5	0.035
50	0.038

Table 1: Simulated average % energy resolution of the RMA for various grid transparencies.

References:

- [1] A. Khursheed, H. Q. Hoang, and A. Srinivasan, *Journal of Electron Spectroscopy and Related Phenomena*, vol. 184, pp. 525-532, 2012.
- [2] H. Q. Hoang and A. Khursheed, *Nuclear Instruments and Methods in Physics Research Section A: Accelerators, Spectrometers, Detectors and Associated Equipment*, vol. 635, pp. 64-68, 2011.
- [3] K. H. Cheong, W. Han, A. Khursheed, and K. Nelliyan, *Microscopy and Microanalysis*, vol. 21, pp. 142-147, 2015.
- [4] C. Integrated Engineering Software Inc, "Lorentz-EM v9.2, Three dimensional Particle Trajectory Solver (Hybrid)," ed, 2014.

ANNULAR FOCUSED ELECTRON BEAM ABERRATION CORRECTORS

A. Khursheed* and W. K. Ang

Department of Electrical and Computer Engineering, National University of Singapore,
4 Engineering Drive 3, Singapore 117576.

*e-mail: eleka@nus.edu.sg

Electron beam core lenses are round lenses which have an electrode on the rotational axis of the lens, a region in which a conventional electron beam usually travels through. However, by use of an annular aperture, that region can be made beam-free, making it then possible to circumvent Scherzer's theorem of being limited by round lens axial aberrations. Although core lenses have been previously proposed as a means for aberration correction [1,2,3,4], they have as yet not led to successful aberration correctors. This paper describes how multi-stage core lens aberration correctors might become a simpler means for aberration correction than the present three-dimensional multipole field approach. Preliminary direct ray tracing simulations carried out here indicate that they can potentially improve the spatial resolution of conventional scanning electron/ion beam focused probe instruments by over an order of magnitude for the same probe current. Simulation examples illustrating how a corrector unit consisting of an annular aperture together with a three-stage core lens unit can significantly reduce the geometric and chromatic aberrations of focused electron/ion beam instruments will be presented.

Figure 1 shows direct ray tracing of electrons through an electric Einzel objective lens test example with an annular aperture/three-stage core lens aberration corrector by using the Lorentz 2EM boundary element software [5]. Eleven 10 keV electron trajectory ray paths uniformly distributed within the emission angular spreads of ± 0.6 mrad around an initial semi-angle of 7 mrad are traced from a point source at the second order geometric aberration correction condition. They are focused by the Einzel objective lens to a working distance of 5.25 mm with a final semi-angular spread of ± 2 mrad around a semi-angle of 23.92 mrad. The lens electrode voltages were systematically adjusted in order to minimize the final probe size.

Figure 2 compares the final probe radius as a function of final semi-angle with that of a comparable hole-aperture beam for the same probe current. Additional ray paths for the energies of 10 keV -0.25 eV and 10 keV + 0.25 eV are also plot. The predicted RMS probe radius at 10 keV for the comparable hole-aperture column is over an order of magnitude bigger than that of the geometric aberration corrected annular focused beam: 97 nm and 2 nm respectively. The radii for the apertures are $R_0 = 75.65 \mu\text{m}$ for the circular aperture and $R_1 = 132.77 \mu\text{m}$ and $R_2 = 152.81 \mu\text{m}$ for the annular aperture. Assuming the source is a coherent one (field emission), the diffraction aberration limited radius for the ring focused beam containing 50% of the total probe current in this case is predicted to be approximately 1 nm. The overall probe size in this case is limited primarily by chromatic aberration which enlarges the simulated probe RMS radius to 6.4 nm.

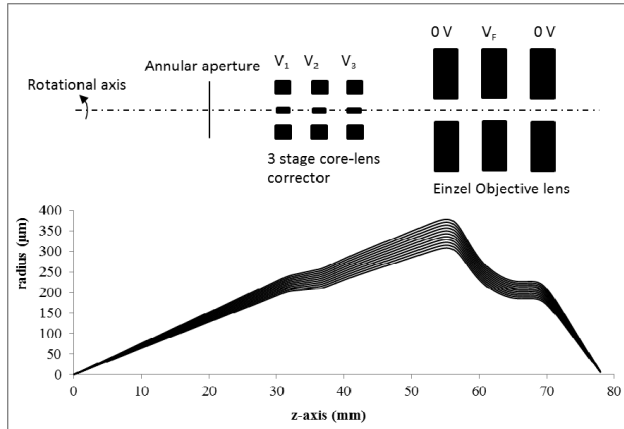


Figure 1 Direct ray tracing of electrons through an electric Einzel objective lens test example with an annular aperture/three-stage core lens aberration corrector

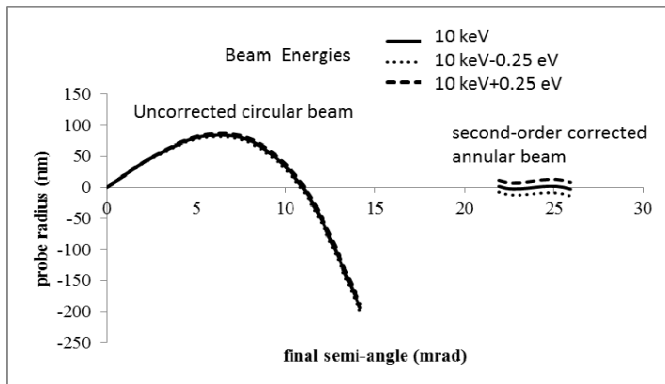


Figure 2 Simulated probe radius as a function of final semi-angle through the electric Einzel objective lens test example with and without the annular aperture/core lens corrector for the same beam current

References:

- [1] F. Lenz and A. P. Wilska, *Optik* 24 (1966/67) 383.
- [2] H. Ito, Y. Sasaki, T. Ishitani, Y. Nakayama, US Patent 7,947,964 B2, May 24th, 2011.
- [3] A. Takaoka, R. Nishi and H. Ito, *Optik*, 126 (2015) 1666-1671.
- [4] C. Own, A. Bleloch, and P. J. Dabrowski, US Patent, US8324574B2, 4th December, 2012.
- [5] LORENTZ-2EM, Integrated Engineering Software Inc., Canada.

FIELD EMISSION FROM THE SURFACE OF HIGHLY ORDERED PYROLYTIC GRAPHITE

A. Knápek, Z. Pokorná

¹Institute of Scientific Instruments of the CAS, v. v. i., Královopolská 147, 612 64 Brno, Czech Republic, e-mail: knapek@isibrno.cz

This paper deals with the electrical characterization of highly ordered pyrolytic graphite (HOPG) surface based on field emission of electrons. The effect of field emission (as illustrated by fig. 1), occurs only at disrupted surface, i.e. surface containing ripped and warped shreds of the uppermost layers of graphite. These deformations provide the necessary field gradients which are required for measuring tunneling current caused by field electron emission. Results of the field emission measurements are correlated with other surface characterization methods such as scanning near-field optical microscopy (SNOM) or atomic force microscopy. A simple method utilizing the field emission of electrons has been devised to characterize the sample surface. Electron and probe microscopies were used to determine the structure of both the bulk sample and the partially exfoliated shreds of the uppermost layers of graphite in locations where field emission is observed.

Using various methods of surface characterization we obtained additional information about the properties of the Highly Ordered Pyrolytic Graphite exhibiting field emission. The morphology of the shreds on the HOPG surface was demonstrated by SEM (fig. 2). Precise information about the height of surface details was obtained by AFM (fig 3.). The presence of subwavelength structures in the near-surface area of the sample was confirmed by SNOM. The comparison of the images taken using SNOM, SEM and AFM allowed us to characterize shreds of multi-layered graphite structure on the surface of HOPG. In our method, the occurrence of the field emission of electrons acts as an indicator of disrupted HOPG surface. Since there are multiple electron sources with various sizes and threshold voltages, the Fowler-Nordheim plot is not linear and so the F-N theory cannot be applied in the entire voltage range. It can only serve for the confirmation of electron tunneling because of the initial linear part of the F-N plot.

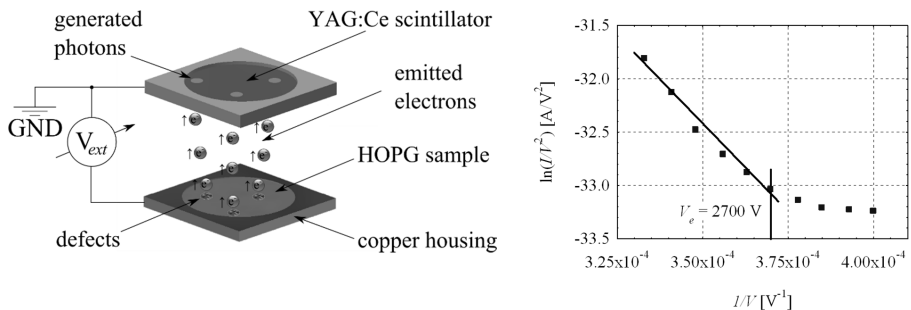


Figure 1 Experimental setup; the HOPG sample is connected to the negative dc source and the YAG scintillator is grounded, serving as an extractor electrode (left) and corresponding F-N plot (right).

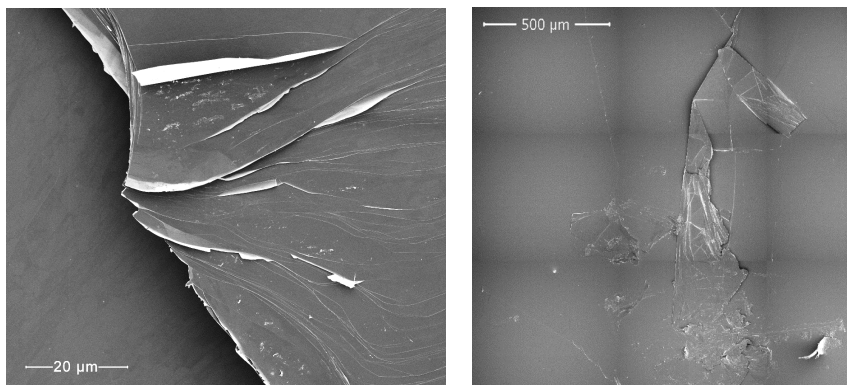


Figure 2 SEM image of the HOPG surface. An overview of the sample surface (left) and typical example of ridge-like morphological structures with interspersed peak-like structures on the sample surface (image right).

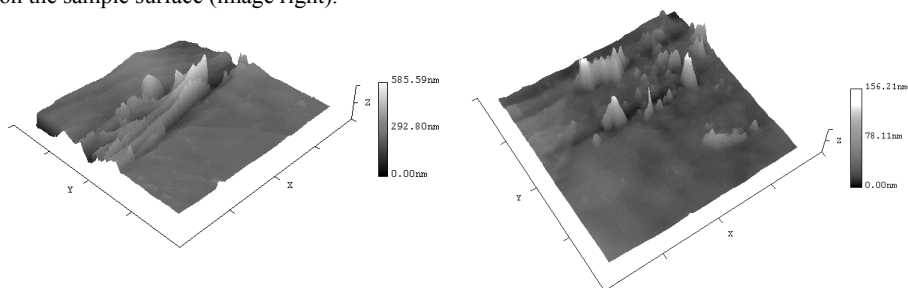


Figure 3 AFM topography image of the HOPG surface showing the height of surface features. A typical example of ridge-like morphological structures on the sample surface (image left); and peak-like structures (right). In both cases, the field of view is $30 \times 30 \mu\text{m}$ wide.

References:

- [1] Mullerova, I., Frank, L. Scanning low-energy electron microscopy. *Advances in imaging and electron physics* **128** (2003): 310-445.
- [2] Bauer, E. Low energy electron microscopy. *Reports on Progress in Physics* **57.9** (1994): 895.
- [3] Forbes, R.G., Edgcombe, C.J. and U. Valdrè. Some comments on models for field enhancement, *Ultramicroscopy*. **95** (2003) 57–65.
- [4] Ivanov, I.G., Hassan, J.U. , Iakimov, T., Zakharov, A.A., Yakimova, R., and E. Janzén. Layer-number determination in graphene on SiC by reflectance mapping, *Carbon*. **77** (2014) 492–500.
- [5] Skulason, H.S., Gaskell, P.E. and T. Szkopek. Optical reflection and transmission properties of exfoliated graphite from a graphene monolayer to several hundred graphene layers, *Nanotechnology*. **21** (2010) 295709.
- [6] The research was financially supported by the Technology Agency of Czech Republic project No.TE01020118.

SEM LEEM – NEW TYPE OF ELECTRON MIRROR MICROSCOPY

V. Kolařík*, P. Jánský and M. Mynář

DELONG INSTRUMENTS a.s., Palackého třída 153b, 61200, Brno, Czech Republic

*e-mail: vladimir.kolarik@delong.cz

LEEM is a well established method for the imaging of surfaces of materials using the impact of very slow electrons (down to zero energy - mirror microscopy). On the other hand, scanning electron microscopy has not consistently solved the detection of electrons in the mirror mode, i.e. in the incident energy range of 3 to 0 eV.

Since mirror microscopy can be realized only when using immersion lenses, the detector in the scanning mode has to capture fast electrons with energy in principle of the same value as of the primary beam. Such “signal” electron beam moves back through the optical system very close to its optical axis and standard rotationally symmetric electron optics is in principle not able to provide their detection. The higher magnification is used, the more signal electrons are lost.

One solution is to use a rotationally asymmetric imaging and detecting system that provides separate beam lines of primary and signal beams [1] as for example magnetic prisms, which are able to compensate for any aberrations of the second order and also for energy dispersion in a symmetrical arrangement [2]. In the asymmetric arrangement, we can reach sufficiently large beam deflection angles (90°) having the energy dispersion of the order of units of micrometers per volt.

The first experiments verifying the correctness of the concept were made with help of an assembly consisting of an (Schottky) electron source equipped with a magnetic gun lens followed by detector unit and electrostatic triode objective lens. The results presented here are demonstrating the ability of the detector to distinguish between BSE and SE even for landing energy 0.5 eV. The integral detector is mixing both signals better showing the mirror character of the image.

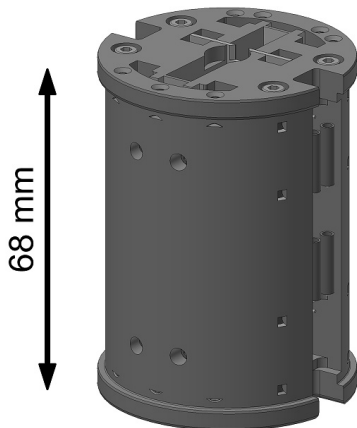


Figure 1 Prism physical set-up.

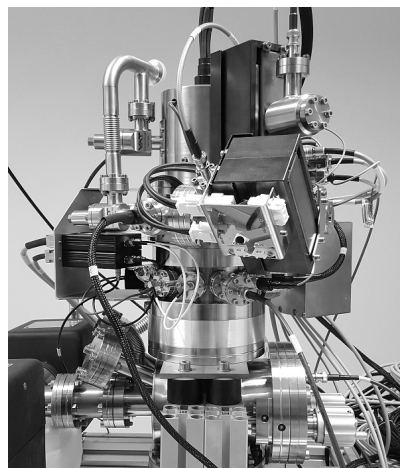


Figure 2 Experimental SEM LEEM

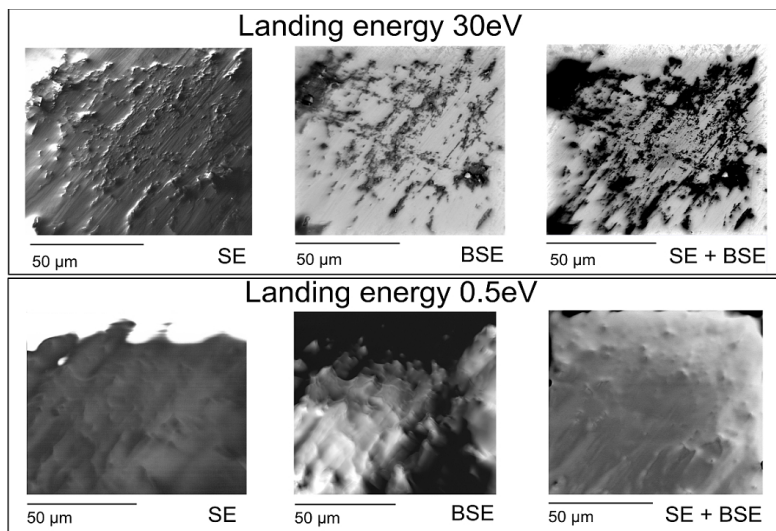


Figure 3 Preliminary results.

References:

- [1] P. Kruit, in *Advances in Optical and Electron Microscopy*, vol. 12, ed. by T. Mulvey (Academic, London, 1991), pp. 93-137
- [2] V. Kolarik, M. Mankos, L. H. Veneklasen, *Optik* 87, No. 1 (1991) 1 - 12

LARGE-AREA GRAY-SCALE STRUCTURES IN E-BEAM WRITER VERSUS AREA CURRENT HOMOGENEITY AND DEFLECTION UNIFORMITY

V. Kolařík^{1*}, M. Horáček¹, M. Matějka¹, S. Krátký¹ and J. Bok¹

¹Institute of Scientific Instruments AS CR, Královopolská 147, 612 64 Brno, Czech Republic
*e-mail: Vladimír.Kolarik@isibrno.cz

The high stability and good current homogeneity in the spot of the e-beam writer is crucial to the exposure quality, particularly in the case of large-area structures when gray-scale lithography is used. Even though the deflection field distortion is calibrated regularly and beam focus and beam astigmatism is dynamically corrected over the entire deflection field, we can observe disturbances in the exposed relief for both nowadays types of e-beam writers, the shaped e-beam writing system and the Gaussian e-beam writing system. A stable and homogeneous angular current density distribution in the spot is important especially in the case of shaped e-beam lithography systems. A non-homogeneity of the spot over deflection field is seen alongside the field boundaries of both lithography systems.

In order to analyze and periodically monitor the two-dimensional current density distribution in the shaped e-beam writer, the four measurement methods for the two-dimensional mapping of the current density distribution in variable-shaped spot were developed and mutually experimentally compared. 1) The method of scanning over a Faraday cup opening utilizes an aperture over which a spot/stamp of a fixed size is scanned in two perpendicular directions. The electron current passing through the opening is collected by the Faraday cup and measured by the pA-meter. 2) The knife-edge method using a forming system utilizes the shaping shutters of the stamp forming system to select step by step the appropriate parts of the e-beam which are sequentially measured by the Faraday cup [1]. 3) The screen irradiation method uses a phosphor screen in order to convert the energy of the e-beam electrons into visible light. The image of the light intensity which is directly proportional to the e-beam current is then recorded by a CCD camera. 4) The electron resist exposure method is based on evaluation of the developed electron resist. The depth of the resist is proportional to the spread of the deposited energy in the electron resist, and is therefore proportional to the e-beam current [2].

The forming system for the creation of rectangular stamps from the original circular e-beam and the measured current density distribution for described measurement methods can be seen in Fig. 1. The knowledge of the current density distribution in the stamp enables the selection of a homogeneous part from the original e-beam and enables to consider the rate between the exposure quality and the writing speed.

We investigated intensively the impact of the above mentioned e-beam exposure imperfections on the visual performance of Diffractive Optical Variable Image Devices (DOVID's). Benchmarking exposures were performed using the Tesla BS600 pattern generator set up in TZ-0 mode [3]. Some other kind of optical gratings were proposed recently for the benchmarking purposes [4]. Several methods seeking to reduce the typical visual squaring (Fig. 2) of e-beam originated optical devices were developed and verified. They are based essentially on the proper main-exposure-field size and shape selection and also on the appropriate rectangular-stamp size and aspect ratio. One selected example is shown in Fig. 3.: two similar benchmark exposures with a different stamp aspect ratio gives visually distinguishable results.

References:

- [1] Bok J. et al., *J. Vac. Sci. Technol. B* 31 (2013) 031603.
 [2] Bok J. et al., *Microelectronic Eng.* 149 (2016) 117-124.
 [3] Kolařík V. et al., *in Proc's of Recent Trends 2012*, ISBN 978-80-87441-07-7, 37-38.
 [4] Meluzín P, et al., *in Proc's of Nanocon 2014*, ISBN 978-80-87294-55-0, 246-251.
 [5] The research was supported by the TACR project TE 01020233, by MEYS CR (LO1212), its infrastructure by MEYS CR and EC (CZ.1.05/2.1.00/01.0017) and by ASCR (RVO:68081731). Acknowledgement to both Mr. Král for exposure tests performed and Ms. Giričová for photos in Fig's 2 and 3.

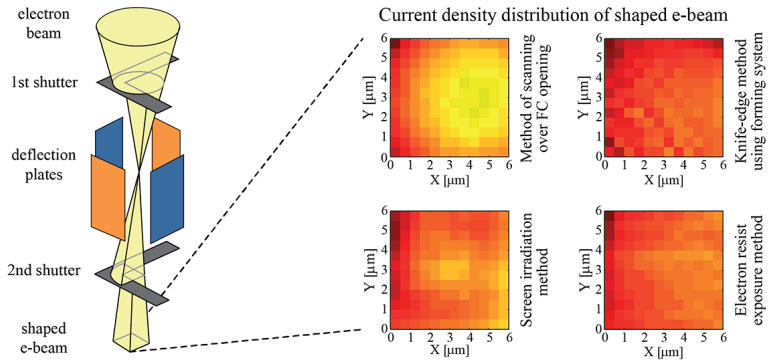


Figure 1 The scheme of the stamp forming system (left) and the current density distribution in a $6 \times 6 \mu\text{m}^2$ e-beam stamp measured with (a) the method of scanning over a Faraday cup opening, (b) the knife-edge method using a forming system, (c) the screen irradiation method, and (d) the electron resist exposure method (right).

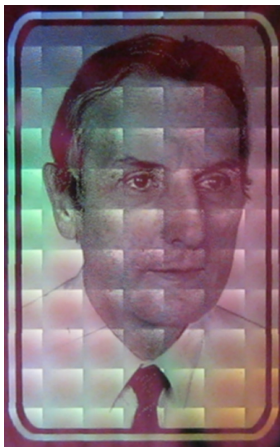


Figure 2 The benchmark exposure test $32 \times 20 \text{mm}^2$; main expo field $3 \times 3 \text{mm}^2$.

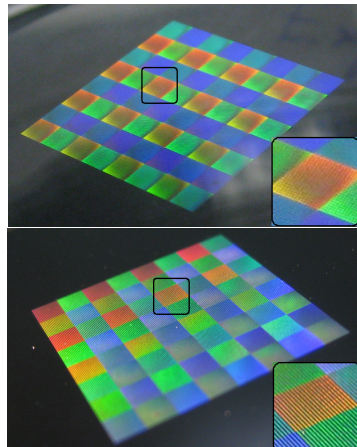


Figure 3 The benchmark exposure test $16 \times 16 \text{mm}^2$; main expo field $2 \times 2 \text{mm}^2$: stamp size ratio (above) $\sim 7.4 : 1$ and (below) $\sim 4.7 : 1$.

BANDPASS FILTER FOR SECONDARY ELECTRONS IN SEM - SIMULATIONS

I. Konvalina*, F. Mika, S. Krátký and I. Müllerová

Institute of Scientific Instruments of the CAS, v. v. i., Královopolská 147, 612 64, Brno, Czech Republic

*e-mail: ivo.konvalina@isibrno.cz

Scanning electron microscope (SEM) is commonly equipped with a through-the-lens secondary electron detector (TLD). The TLD detector in Magellan 400 FEG SEM [5] works as a bandpass filter for the special setup of potentials of electrodes inside the objective lens, the positive potential on the specimen regulates the energy window of the filter. An energy filtered image contains additional information to that of an unfiltered one. The contrast of the filtered image is changed and new information about the topography and the material can be observed [1,2].

To understand image contrast formation with TLD detector we traced SEs and BSEs through the three-dimensional (3D) model of included 3D distribution of the electrostatic and magnetic fields. The properties of the bandpass filter were simulated for a working distance (WD) in the range of 1 mm to 3 mm and a primary beam energy (E_p) from 1 keV to 10 keV. The 3D electrostatic field of the system was calculated by Simion [3], magnetic field and raytracing were done using EOD program [4].

The cross section of the 3D arrangement used in simulation is shown in Figure 2a. In the objective lens there are several electrodes that help to SEs travel in direction on the scintillator. At first SEs emitted from the specimen are attracted into the objective lens (OL) by the “suction tube” electrode that is positively biased. Electrostatic field in the OL that is created by the “push electrode” (is not visible in Figure 2a) and “mirror electrode” deflects SEs towards scintillator. In the simulation we used fixed potentials of suction tube ($U_{ST} = +150$ V), push electrode ($U_{PE} = -140$ V), mirror electrode ($U_{ME} = +20$ V) and scintillator ($U_{SC} = +10$ kV), the potential on the specimen vary from 0 V to 16 V, with the step of 4 V. The intensity of the magnetic field is determined by the primary beam energy and working distance. The objective lens works in immersion mode, the specimen is placed in strong magnetic field that collimates emitted electrons into objective lens.

The energy of SEs changing from 1 eV to 30 eV with a step of 1 eV, the polar angle from 0° to 90° with a step of 1° and the azimuthal angle from 0° to 360° with a step of 10° . The TLD system is asymmetrical to the optical axis, for that reason we study also the azimuthal angle for that SEs escape the specimen. One example of simulated results for potential on the specimen $U_{SB} = +4$ V is shown in Figure 1, where the initial polar angle θ_0 and initial azimuthal angle ϕ_0 are shown as a function of the initial energy of electron E_0 .

The emission energy of SEs detected by the TLD with taking into account the cosine distribution of emission is shown as a function of the positive sample bias (Figure 2b). For each point on the curves in the graph we have to trace 98 280 particles. The lower (min) and

upper (max) thresholds of the bandpass filter define the energy region that TLD detector detects SEs in the whole range of emitted polar and azimuthal angles.

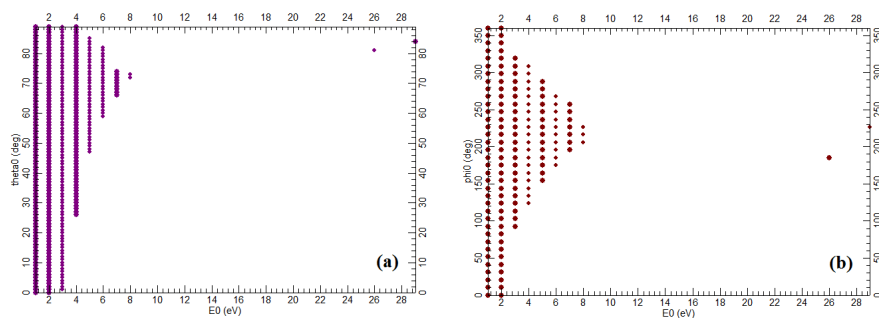


Figure 1 The initial polar angle θ_0 (a) and initial azimuthal angle ϕ_0 (b) as a function of the initial energy of electron E_0 , $E_P = 1$ keV, $WD = 1$ mm, $U_{SB} = +4$ V.

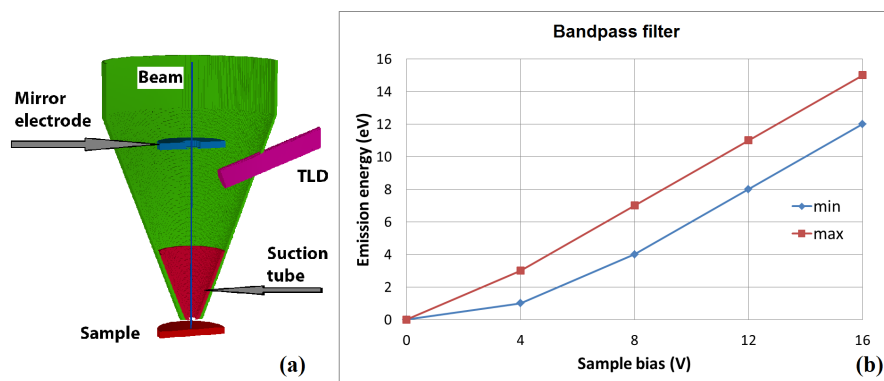


Figure 2 Arrangement used for simulation (a). The emission energy of SEs detected by the TLD as a function of the sample bias, working distance $WD = 1$ mm, primary beam energy $E_P = 1$ keV (b).

References:

- [1] Kazemian P., Mentink S.A.M., Rodenburg C. and Humphreys C.J., *Ultramicroscopy* **107** (2007), p. 140-150.
- [2] Cazaux J., *Journal of Electron Microscopy* **61** (2012), p. 261-284.
- [3] Dahl D.A., *Int. J. Mass Spectrom.* **200** (2000) p. 3-25.
- [4] Zlámál J. and Lencová B., *Nucl. Instr. Meth. Phys. Res. A* **645** (2011), p. 278-282.
- [5] <http://www.fei.com/>
- [6] The work is supported by the TA CR (TE01020118), MEYS CR (LO1212), its infrastructure by MEYS CR and EC (CZ.1.05/2.1.00/01.0017) and by CAS (RVO:68081731). The authors would like to thanks Dr. M. Unčový (FEI Company, Brno, Czech Republic) for useful discussions.

ELECTRON MANIPULATION WITH LIGHT – ACCELERATION, STREAKING AND FOCUSING OF SUB-RELATIVISTIC ELECTRONS

M. Kozák^{1,*}, J. McNeur¹, N. Schönenberger¹, A. Li¹, A. Tafel¹, and P. Hommelhoff¹

¹ Department of Physics, Friedrich-Alexander-Universität Erlangen-Nürnberg (FAU), Staudtstrasse 1, 91058 Erlangen, Germany, EU

² Max-Planck-Institute for the Science of Light, Günther-Scharowsky-Str. 1, 91058 Erlangen, Germany, EU

*e-mail: martin.kozak@fau.de

In this contribution we review the latest experimental research of the interaction between optical near fields and sub-relativistic electrons. Its principle is based on energy and/or transverse momentum exchange between electrons and the near-field diffraction mode of light generated by a femtosecond laser pulse at a periodic dielectric nanostructure. This so-called inverse Smith-Purcell effect was theoretically predicted shortly after the invention of the laser [1]. However, its first experimental demonstration was only realized in 2013 [2]. In the same time, similar experimental scheme was used to accelerate relativistic electrons [3]. The observation of electron energy modulation by light opened a window for several interesting applications of this effect in the fields of dielectric laser acceleration (DLA) [4,5,6,7] and sub-optical-cycle manipulation and temporal gating of electron beams [8].

When nonlinear forces are negligible, it is not possible to impart energy or momentum to an electron in vacuum by light. This is a consequence of energy and momentum conservation laws. However, if we introduce a boundary for the light field, the spatial symmetry is broken and energy flow between oscillating fields and electrons becomes possible. To achieve an efficient energy exchange, an approach similar to radio-frequency (RF) accelerators can be realized. In the RF case a standing wave with a strong longitudinal field component is excited in the periodic series of cavities. The standing wave can be decomposed to two travelling waves propagating in opposite directions. If the electron velocity is synchronized with the phase velocity of one of the travelling waves, it can become accelerated. The effect is linear with the applied field and the final electron energy depends on its injection phase with respect to the oscillating field.

The field amplitude which can be realized in the GHz frequency range in RF accelerators is limited to 50-100 MV/m by the electric breakdown phenomena occurring on the inner surface of the accelerator tube. To achieve stronger accelerating fields and thus to reach higher acceleration gradients, the oscillation frequency of the field can be increased by a factor of 10^5 by using light as a driving field. Instead of the metallic or superconductive cavities in RF-based accelerators, wide bandgap transparent dielectric nanostructures are used as a spatial boundary for the field in DLA. Due to low absorption in the visible/near-infrared spectral window and due to the short duration of femtosecond driving laser pulses, the energy density dissipated at the structure is small, allowing to reach substantially higher field amplitudes before the laser damage occurs (several GV/m).

Not only the extreme strength of the synchronous field, but also the sub-optical-cycle energy structure imprinted to the electron beam can be interesting for applications in ultrafast

electron diffraction and microscopy, as well as for ultrashort electron bunch metrology. Here we present a series of demonstration experiments. We visualize the sub-cycle energy structure in the time domain by using two subsequent laser-electron beam interactions and demonstrate electron transverse streaking and focusing. Experiments are performed using a sub-relativistic electron beam generated in a scanning electron microscope (SEM) column at energies of 25-30 keV.

The sub-cycle energy structure imprinted to the electron beam during its interaction with optical near-fields is characterized via two spatially and temporally separated laser pulses. By changing the relative phase between the two driving fields, the accelerated electron reveals phase oscillations, directly demonstrating the time structure of the energy modulation of the final electron distribution. As we show theoretically, this effect can be used for temporal gating of electron bunches with sub-cycle temporal resolution (approaching $1 \text{ fs} = 10^{-15} \text{ s}$ already) [8].

In a related experiment we generate transverse forces by changing the experimental geometry and tilting the grating with respect to the electron beam. This leads to a phase-dependent transverse streaking of electrons by light. Due to the linear dependence of the transverse momentum gain on the oscillating laser field, a light driven streak camera for ultrashort electron bunches can be constructed based on this principle, with a theoretical resolution of $10 \text{ as} = 10^{-17} \text{ s}$ [8].

The maximum transverse force which can be applied to the propagating electron depends linearly on the tilt angle of the grating. We use this fact to build a focusing element, where the tilt angle changes linearly with the distance from the electron beam center. We experimentally demonstrate that this element can be used for simultaneous electron acceleration and focusing with focal distances as short as $150 \mu\text{m}$ [7].

The results demonstrated here will lead to a number of new applications in which the ultrafast manipulation of tightly focused electron beams by light will play a crucial role.

References:

- [1] K. Shimoda, *Appl. Opt.* **1** (1962), 33-35.
- [2] J. Breuer, and P. Hommelhoff, *Phys. Rev. Lett.* **111** (2013), 13480.
- [3] E. A. Peralta et al., *Nature* **503** (2013), 91-94.
- [4] R. J. England, et al., *Rev. Mod. Phys.* **86** (2014), 1337-1389.
- [5] K. J. Leedle, R. Pease, and R. L. Byer, *Optica* **2** (2015), 158-161.
- [6] J. Breuer, R. Graf, A. Apolonski, and P. Hommelhoff, *Phys. Rev. STAB* **17** (2014), 021301.
- [7] J. McNeur, et al., arXiv:1604.07684 (2016).
- [8] M. Kozák, et al., arXiv:1512.04394 (2015).

ELECTRON GRATING MIRROR FOR QUANTUM ELECTRON MICROSCOPY

M.A.R. Krielaart* and P. Kruit

TU Delft Department of Imaging Physics, Lorentzweg 1, 2628 CJ, Delft, The Netherlands

*e-mail: m.a.r.krielaart@tudelft.nl

One of the components that is required for the recently proposed quantum electron microscope is a two-state coupler or coherent electron beam-splitter [1]. This is an electron-optical device that separates an incident electron wave in different components. Among the suggested methods to achieve this goal is the novel concept of an electron grating mirror. Such device acts as a mirror for an incident plane wave front. By placing a periodic structure on the mirror surface, the nearby equipotential lines are curved in space. This curvature is expected to induce a periodic phase shift within the beam. As a result, diffraction occurs in the reflected beam in a similar way as in a light-optical grating. The diffraction pattern can be imaged back onto the sample (Fig. 1).

The mirror surface is kept at a negative potential just below that of the electron energy to prevent the electrons from hitting the sample. The field strength is controlled by placing a grounded silicon aperture plate at 200 μm above the mirror. As this results in a diverging lens effect an additional lens is required to provide a focussing action toward the sample again.

The relative phase shift in the beam is gradually introduced within the periodic retarding field near the mirror surface. This is different from the light optics case, where interaction at a grating causes an instantaneous phase shift. For the analysis of the phase shift, the WKB approximation is valid since the electron wave length is much smaller than the mirror period:

$$\Delta\phi(x) = \int \frac{2\pi}{\lambda(x, z)} dz \quad \text{with} \quad \lambda = \frac{h}{\sqrt{2meU(x, z)}}.$$

The potential U at the mirror plate with pattern amplitude δ is approximated by a cosine potential. The potential near the mirror is then found as a solution to the Laplace equation:

$$U(x, z) = E_z(z - z_0) - E_z\delta \cos\left(2\pi\frac{x}{d}\right) \exp\left\{-2\pi\frac{z}{d}\right\}.$$

Here, z_0 is the separation between the mirror and aperture and E_z the field strength. Initial calculations with the above assumptions show that a large field strength and large grating period is required to obtain a similar phase contrast for a range of electron energies. When the mirror is positioned below the sample in a SEM, this results in multiple images that are obtained simultaneously. First there is the conventional image due to the secondary electrons. In the presence of the mirror, also the bottom of the sample is probed with the reflected and diffracted beams. The secondary electrons generated by these beams are recorded simultaneous as well, thus resulting in multiple superposed images. The effect of the

diffracted beams on the sample should be visible as fringes on the mirror image generated by the reflected beam.

Preliminary (not published) experiments already showed the imaging of a such sample by using a flat electron mirror.

Currently, grating mirrors are prepared in our lab. This grating mirror consists of a silicon substrate. Patterning of the grating structure is done by Focused Ion Beam (FIB) lithography. Rectangular patterns with period in the range 800 – 2200 nm are produced in this fashion, all with a profile depth of 800 nm and frontal area of approximately $30 \times 30 \mu\text{m}^2$.

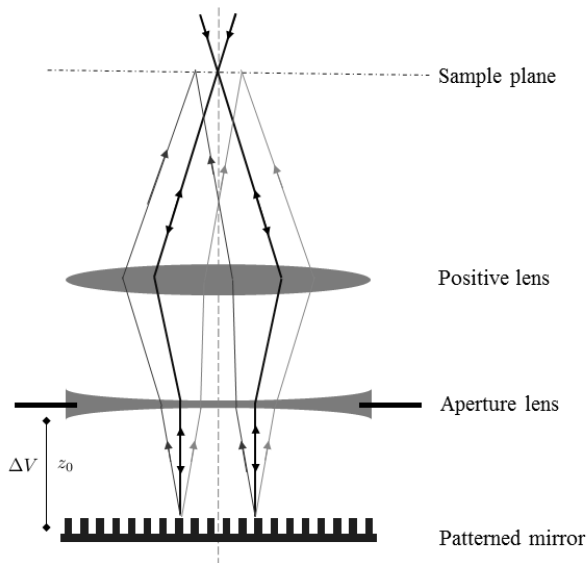


Figure 1 Schematic working principle of the grating mirror. The beam is focussed at the sample, generated secondary electrons are detected and diverges below. The magnetic lens provides the focussing power to counteract the divergence due to the mirror-aperture field. This result in a parallel beam above the mirror plane and also focusses the reflected and diffracted wave components back to the sample. Again secondary electrons are generated and detected as well. This results in a superposition of images. The presence of the diffraction spots is observed by fringes around features for the mirror image.

References:

[1] Kruit P., Hobbs R.G., Kim C-S., Yang Y., Manfrinato V.R., Hammer J., Thomas S., Weber P., Klopfer B., Kohstall C., Juffmann T., Kasevich M.A., Hommelhoff P., Berggren K.K., *Ultramicroscopy* **164** (2016), p. 31-45.

NEW DETECTORS FOR LOW-ENERGY BSE

O. Lalinský¹, P. Schauer¹, M. Kučera², M. Hanuš², Z. Lučeničová²

¹Institute of Scientific Instruments of the CAS, Královopolská 147, 612 64 Brno, Czech Republic

²Charles University, Faculty of Mathematics and Physics, 121 16 Prague, Czech Republic

*e-mail: xodr@isibrno.cz

Backscattered electrons (BSE) are mostly used to study the specimen's topography. Nowadays, low energy (units of keV) electron beam imaging is often necessary for example for the research of nanomaterials, biomaterials or semiconductors. Because BSE detectors are mostly non-accelerating or low-accelerating, electrons with approximately the same energy as primary beam (PB) have to be detected. Therefore, BSE detectors need to become optimized for such low-energy electrons. For the scintillation detectors, the biggest problem probably lies in the scintillator. Semiconductor detectors aren't studied in this work. Cerium activated bulk single crystals of yttrium aluminium garnet (YAG:Ce) $Ce_xY_{3-x}Al_5O_{12}$ are widely used as scintillators for the detection of high-energy backscattered electrons (BSE). However, commonly used YAG:Ce single crystal strongly loses its light yield (LY) with the decrease of the PB energy [1]. As possible available alternatives for this application, bulk single crystals of yttrium aluminium perovskite (YAP:Ce) $Ce_xY_{1-x}AlO_3$ and CRY018 can be predicted. However, similar LY drop can be expected also with these scintillators.

There are two main reasons, why this occurs. Firstly, slower electrons don't have enough energy to pass through the relatively thick standard conductive layer on the scintillator surface. Therefore, thinner conductive layer has to be used. Secondly, commonly available scintillators suffer from structural defects that are created mostly due to surface damage (as a result of its grinding, polishing, purification or contamination) or already during the own bulk Czochralski growth. The influence of all of these defects on cathodoluminescence (CL) properties can be eliminated by the scintillators in form of thin single crystalline films because, as shown previously [2], the concentration of these defects decreases with the decreasing temperature of the crystal growth. Therefore, single crystalline epitaxial films have attracted a lot of attention recently because the growth temperature of these films is about a half (1000 °C) of the bulk ones (2000 °C). Moreover, appropriate doping of the garnet structure can suppress the influence of the defects on the CL properties.

For the purpose of this work, bulk Czochralski grown single crystals of YAG:Ce, YAP:Ce and CRY018 were studied. Results were compared with those of promising cerium activated single crystalline films of gadolinium aluminium gallium garnet (GAGG:Ce) $Ce_xGd_{3-x}Ga_yAl_{5-y}O_{12}$. These films were grown by the isothermal dipping liquid phase epitaxy onto YGG substrates from lead-free BaO-B₂O₃-BaF₂ flux [3]. These specimens were coated with conductive layers of different composition and different thicknesses. Properties of these layers are in the table shown in Table 1.

The specimens were excited by an electron beam with energy in range from 0.8 to 10 keV using a specialized CL apparatus [4]. In this energy range, CL LY of YAG:Ce were measured for coating layers of different composition and different thicknesses (Fig. 1). Moreover, CL spectra have been measured for all presented specimens (Fig. 2).

It was shown, that the coating layer with thickness of only units of nm has to be used to allow low-energy BSE penetrating the layer without significant losses. Moreover, it was shown, that the GAGG:Ce film with balanced Ga content shows excellent scintillation properties where the effect of unwanted structural defects was suppressed, the spectrally corrected CL LY value exceeded 160 % of the commercially available bulk YAG:Ce single crystal, and CL decay was dominated by a fast component with 50 ns decay time which is close to that of Ce^{3+} (5d-4f) photoluminescence decay. Thanks to these excellent CL properties at PB energy of 10 keV, GAGG:Ce single crystalline films are new prospective scintillators suitable for low-energy BSE detectors. This research is in progress, therefore other results at different PB energies will be presented at the seminar.

Acknowledgements: The research was supported by the Technology Agency of the Czech Republic (TE01020118), by Czech Science Foundation (projects GA16-05631S, GA16-15569S) and by Ministry of Education, Youth and Sports of the Czech Republic (project LO1212) and by European Commission (project CZ.1.05/2.1.00/01.0017). The authors thank the company CRYTUR, s.r.o., for supplying with the specimens of bulk single crystals.

References:

- [1] G. F. J. Garlick, Brit. J. Appl. Phys. 13 (1962) 541–547.
- [2] M. Nikl, E. Mihokova, J. Pejchal, A. Vedda, Y. Zorenko, K. Nejezchleb, Phys. Status Solidi B 242 (2005) R119–R121.
- [3] M. Kucera, K. Nitsch, M. Kubova, N. Solovieva, M. Nikl, J.A. Mares, IEEE Trans. Nucl. Sci. 55 (2008) 1201.
- [4] J. Bok, P. Schauer, Rev. Sci. Instrum. 82 (2011) 113109.

Film	Atomic number	Atomic weight	Density (g/cm^3)	Thickness (nm)	Trans. of el. of 700 eV (%)
Aluminium (Al)	13	26.98	2.7	3.8	63.2
				5.0	48.0
				10.0	15.1
				15.0	1.3
Scandium (Sc)	21	44.95	2.99	3.0	69.0
				5.0	45.1
Nickel (Ni)	28	58.69	8.91	1.0	74.8
				2.0	50.2
Indium Tin Oxide (ITO)	24.21*	55.11*	7.16	4.0	6.24
				7.0	0.0

*weighted values

Table 1: Properties of commonly used elements for coating layers for scintillators. Data in the last column were simulated by the Monte Carlo method that used the elastic single scattering model with the Mott cross-sections and the Bethe slowing-down approximation.

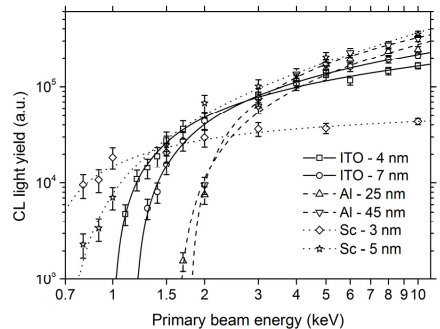


Figure 1 The cathodoluminescence (CL) light yield of the YAG:Ce single crystal scintillator coated with layers of different composition and different thicknesses as a function of the primary beam energy.

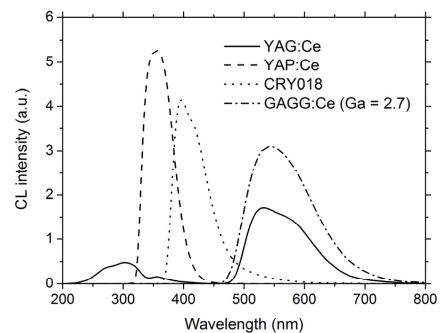


Figure 2 Cathodoluminescence (CL) spectra of $Ce_{0.02}:Gd_3Ga_{2.7}Al_{2.3}O_{12}$ (GAGG:Ce) compared with commercially available YAG:Ce, YAP:Ce and CRY018. Spectra were corrected for the apparatus transmissivity and detector spectral sensitivity. Primary beam energy was 10 keV.

BANDPASS FILTER FOR SECONDARY ELECTRONS IN SEM - EXPERIMENTS

F. Mika, I. Konvalina, S. Krátký and I. Müllerová

Institute of Scientific Instruments of the CAS, Královopolská 147, Brno, Czech Republic.

e-mail: fumici@isibrno.cz

Bandpass energy filtering using a through-the-lens secondary electron (TLD) detector in a field emission gun SEM (FEG-SEM) has been known over a decade. During energy filtering, image contrast is changed and new information about the material can be observed [1]. Our motivation for this study was to compare theoretical calculations with the experimental data of the SE bandpass energy filter in Magellan 400 FEG SEM. The TLD detector works as a bandpass energy filter for the special setup of electrode potentials inside the objective lens, with the positive potential on the specimen regulating the energy window [2].

A sample with chromium and silver stripes on silicon substrate was used for the experiments. The silicon substrate was sputtered by 150 nm of chromium, PMMA resist was spin-coated onto the wafer and the designed pattern was exposed by e-beam writer. After pattern developing, the chromium layer was etched by wet solution and a 150 nm thick silver layer was sputtered. The remaining resist mask was lifted off, resulting in alternating 6 μm wide chromium stripes and 3 μm wide silver stripes. Filtered and unfiltered images of the sample are in Figure 1.

The energy spectrum of electrons emitted from both materials was simulated using Geant4-based [3] software for Monte Carlo simulation of electron-specimen interaction in low-voltage SEM. The primary beam energy was $E_p = 1 \text{ keV}$ and the simulations worked with $N(E_p) = 50\,000$ beam particles. The results of MC simulations for SEs leaving the chromium and silver are shown in Figure 2. The number of SEs emitted from chromium is higher than from silver for energies from 0 to 10.2 eV, for energies higher than 10.2 eV more SEs are emitted from the silver.

We successfully proved the functionality of the filter by taking the images of the test sample with a positive potential of 0, 4, 6, 8, 10, 12, 16 and 24 V on it. We then plotted the intensity of image signals from both materials depending on the sample voltage (Figure 3). For a potential of 8 V on the sample the TLD detects mainly electrons with energies 4 to 7 eV (Figure 1a) [2], which means that both the SE yield and the measured signal intensity of chromium is higher than for silver. On the other hand for a potential of 12 V, TLD detects energy window from 8 to 11 eV [2], and the measured signal intensity for silver stripes is now higher than from chromium (see Figure 3).

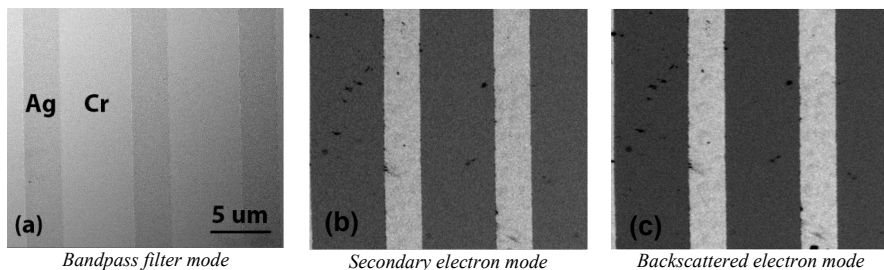


Figure 1 Ag (3 μm)/Cr (6 μm) stripes on a silicon substrate imaged with a TLD detector in different modes. With potentials of (a) + 8 V on the sample and + 150 V on the suction tube; (b) 0 V on the sample and + 70 V on the suction tube; (c) 0 V on the sample and - 150 V on the suction tube.

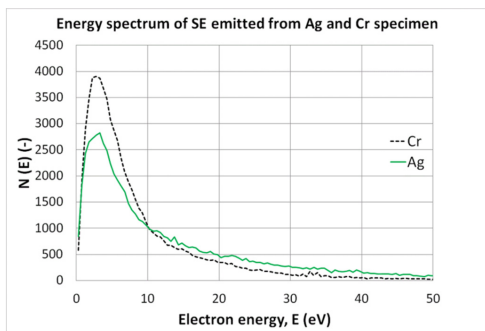


Figure 2 Simulated energy spectrum of secondary electrons for silver and chromium. Primary beam energy $E_p = 1$ keV. Intersection of curves for both materials is at the energy of 10.2 eV.

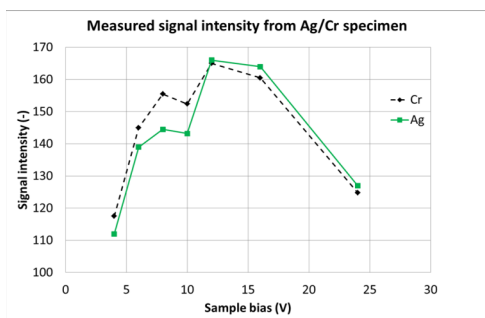


Figure 3 Measured signal intensity from the Ag/Cr sample as a function of the sample bias. Intersection of the signal intensity curves was found at the sample bias of 11.8 V.

References:

- [1] Kazemian P., Mentink S.A.M., Rodenburg C. and Humphreys C.J., *Ultramicroscopy* **107** (2007), p. 140-150.
- [2] Konvalina I., Mika F., Müllerová I. and Krátký S., *Proceedings of the MC 2015*, Göttingen (2015), p. 378-379.
- [3] Kieft E. and Bosch E., *J. Phys. D: Appl. Phys.* **41** (2008), p. 1-10.
- [4] The work is supported by the TA CR (TE01020118), MEYS CR (LO1212), its infrastructure by MEYS CR and EC (CZ.1.05/2.1.00/01.0017) and by CAS (RVO:68081731). Thanks to Dr. M. Unčový (FEI Company, Brno, Czech Republic) for useful discussions.

CORRECTION OF THE CHROMATIC AND SPHERICAL ABERRATION IN LOW-VOLTAGE TRANSMISSION ELECTRON MICROSCOPY

H. Müller¹, M. Linck¹, P. Hartel¹, F. Kahl¹, J. Zach¹, S. Uhlemann¹, J. Biskupek², F. Börrnert², Z. Lee², M. Mohn², U. Kaiser² and M. Haider¹

¹Corrected Electron Optical Systems GmbH, Englerstraße 28, D-69126 Heidelberg, Germany.

²Central Facility of Electron Microscopy, Ulm University, Albert-Einstein-Allee 11, D-89081 Ulm, Germany.

e-mail: mueller@ceos-gmbh.de

During the last decade modern charged-particle optics instrumentation has tremendously improved the resolving power in transmission electron microscopy. Most recently, the simultaneous correction of the chromatic as well as the spherical aberration could be demonstrated [1]. This is extremely useful to image beam sensitive materials consisting of light atoms with low electron energies [2,3]. Within the framework of the Sub-Ångström Low-Voltage Electronmicroscopy (SALVE) project headed by Ulm University [4] we have developed a novel dedicated low-voltage C_c/C_s -corrector for operation at 80 kV to 20 kV. With this instrument e.g. at 40 kV an information limit of 90 pm could be achieved. This is only fifteen times the electron wavelength and corresponds to an effective optical aperture of 67 mrad [5]. Even at 30 kV atomically resolved images of single-layer graphene, MoS_2 , and CNT structures are now possible.

The SALVE C_c/C_s -corrector is based on the quadrupole / octupole principle and consists of eight magneto-static multipole stages, two are capable to produce electro-static quadrupole fields as well. The corrector compensates for the chromatic aberration, the spherical aberration and the off-axial coma of the objective lens, all non-round parasitic aberrations up to the fifth order are corrected as well as all parasitic off-axial aberrations up to the third order. By design the fifth-order spherical aberration can be adjusted to positive values between 2 mm and 5 mm. This enables optimum bright-atom phase contrast for thin specimens with light atoms. Technologically, C_c -correction is very demanding. Superimposed magneto-static and electro-static quadrupole fields with carefully matched fringing fields are necessary. The elements must be placed at a position in the path of rays where the beam has a strongly elongated elliptic cross-section. A symmetric arrangement then is used to cancel out the chromatic astigmatism which is produced simultaneously with the chromatic defocus. In order to achieve a sufficient strength of correction the electro-static fields must be rather strong, in the case of the SALVE corrector we use voltages up to of 8 kV at the electro-static elements. The focusing action of the strong electro-static quadrupole fields is compensated to a large extent by the superimposed magneto-static quadrupole fields. Unfortunately, the resulting stability requirements for the current and high-tension supplies are rather severe [5]. In order to improve the information limit in TEM by reducing the chromatic focus spread from, e.g. $\sigma(C_1) = 25$ nm to almost zero at 20 kV, the parasitic focus spread due to the electronic instabilities of all focusing element has to be very small. In our case we finally could show that the total parasitic focus spread is far below 1.0 nm at 20 kV (Fig. 1b). This is more than sufficient to guarantee that the information transfer in the SALVE instrument is not limited by focus spread anymore and shows that the electronic stability of the most critical current and high tension supplies is better than 50 ppb (rms, fr) in the frequency range down

to 0.1 Hz. The correction of the geometrical aberrations is achieved by magneto-static hexapole, octupole and decapole fields individually excited on the eight multipole stages. During the alignment 104 channels have to be adjusted and controlled. This is only possible by sophisticated semi-automatic alignment procedures. For the final user the complexity of the optical system is almost invisible and the operation is quite similar to that of a normal hexapole-type imaging corrector.

Achromatic imaging in TEM enables the investigation of interface and defect structures at very low voltages with minimized knock-on specimen damage what was not possible before. For energy-filtered TEM now very large energy windows with increased signal can be used without noticeable degradation of image resolution (Fig. 1a). This is encouraging for advanced EFTEM applications and in the near future may produce a demand for further improvements also in the area of in-column or post-column imaging energy filters, since then their residual higher-degree dispersion and chromatic distortions could become the performance limiting factor.

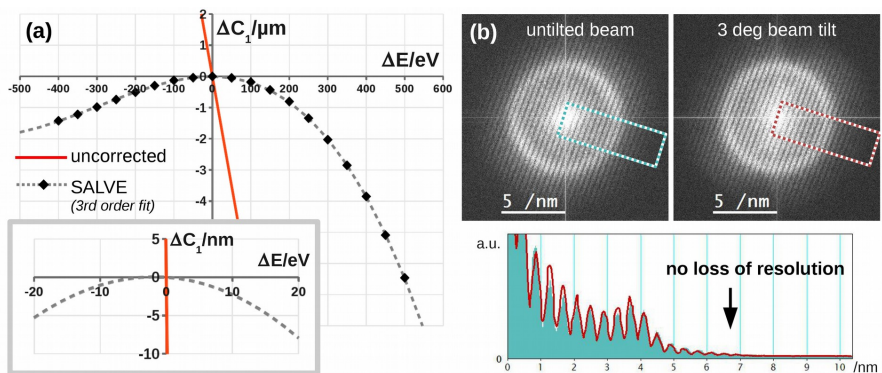


Figure 1 (a) In C_c -uncorrected TEMs (red line: $C_c=1.45$ mm) the defocus changes dramatically with the energy. In the SALVE microscope (black dots: measured, dashed line: third-order fit) the dominant (linear) chromatic aberration is corrected and changes of defocus occur only due to the remaining quadratic and cubic chromatic aberrations. (b) Estimation of focus spread: The information transfer under axial illumination (solid profile) does not show any deterioration even under 3° (52.4 mrad) of beam tilt (red line in profile)

References:

- [1] Haider, M., et al. *Microscopy and Microanalysis* 16.04 (2010): 393-408.
- [2] Egerton, R. F., P. Li, and M. Malac. *Micron* 35.6 (2004): 399-409.
- [3] Kaiser, U., et al. *Ultramicroscopy* 111.8 (2011): 1239-1246.
- [4] URL www.salve-project.de
- [5] Linck, M. et al. *submitted* (2016).
- [6] Haider, M., et al. *Ultramicroscopy* 108.3 (2008): 167-178.

SCANNING TRANSMISSION MICROSCOPY AT VERY LOW ENERGIES

I. Müllerová*, E. Mikmeková, I. Konvalina and L. Frank

Institute of Scientific Instruments of the CAS, Královopolská 147, 612 64 Brno, Czech Republic

*e-mail: ilona@isibrno.cz

To operate down to units of eV with a small primary spot size, a cathode lens with a biased specimen was introduced into the SEM [1] (Fig. 1). The reflected signal, accelerated secondary and backscattered electrons, is collected by detectors situated above the specimen. When we insert a detector below the specimen, the transmitted electron signal can also be used for imaging down to zero energy. Fig. 1 also shows an example of the simulated signal trajectories of electrons that impact on the detector of reflected electrons, based on an Yttrium Aluminium Garnet (YAG) crystal, and trajectories of electrons transmitted through the specimen and incident on a semiconductor detector based on the PIN structure.

Pilot experiments with the high-resolution scanning low-energy electron microscope (SLEEM) were performed on freestanding graphene samples. Fig. 2 shows micrographs taken in the reflected electron (RE) and transmitted electron (TE) modes at several energies. The RE signal was composed of both secondary and backscattered electron emission, accelerated in the cathode lens field toward the detector with the secondary electron contribution diminishing with decreasing energy owing to escape through the detector bore. In the RE frames, the maximum contrast between the graphene and the lacey carbon appears at 1 keV and decreases toward higher and lower energies due to the information depth extending and shortening, respectively. These images show empty holes, but do not reveal thicker islands of graphene. In the TE mode, we see multilayer graphene islands at and below 100 eV which underlines the suitability of the SLEEM for examination of 2D crystals. Some details inverting their contrast more than once (see the arrow) represent interpretation challenges. These may arise from contaminations that become charged.

Traditional counting of graphene layers by Raman spectroscopy is faced by the low lateral resolution of light optical imaging. SLEEM provides much higher resolution, so it is worth checking its selectivity for the same purpose. Fig. 3 shows the contrast of individual graphene layers preserved down to units of eV. Measurement of the transmissivity was calibrated between the zero signals on mesh rungs and the full signal in empty holes, see Fig. 3. Generally, the transmissivity might be expected to grow below some 50 eV because of the inelastic mean free path of electrons steeply extending as verified by experiment and simulations for a large number of materials. This property should also project itself in the transport mean free path governing the transmissivity. However, due to the absence of an energy gap in graphene, the interband electron transition is obviously preserved down to the lowest energies and keeps this scattering mechanism active for reducing the penetration of electrons.

The transmissivity of the graphene samples naturally depends on the cleanness of the surface. We have established that while fast electrons decompose the adsorbed hydrocarbon molecules

creating a carbonaceous contamination layer, below 50 eV the incident electrons release these molecules and leave the surface atomically clean [2,3].

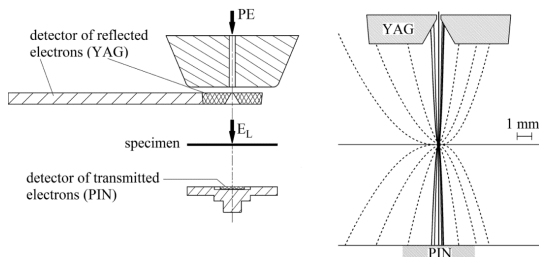


Figure 1 *Left*: the cathode lens assembly. *Right*: an example of the trajectories of the reflected and transmitted signal electrons. The initial energies of electrons are 5 eV (full lines) and 300 eV (dashed lines) in the right half-space, and 10 eV (full lines) and 1,000 eV (dashed lines) in the left half-space. The initial polar angles are 0° , 30° , 60° and 90° with respect to the optical axis. The electrostatic field strength between the detectors and the specimen is 5 keV/7 mm.

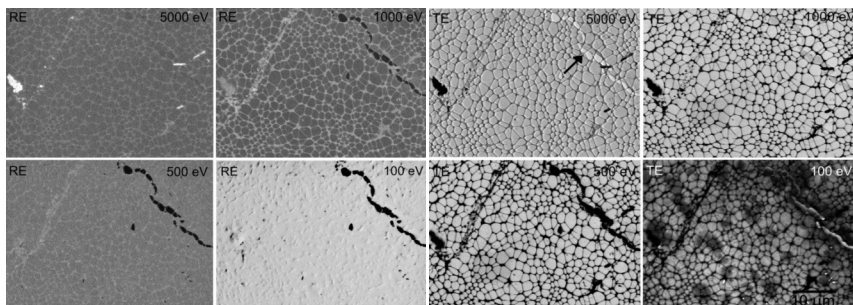


Figure 2 Freestanding sample of 3 to 5 graphene layers imaged in reflected and transmitted electrons.

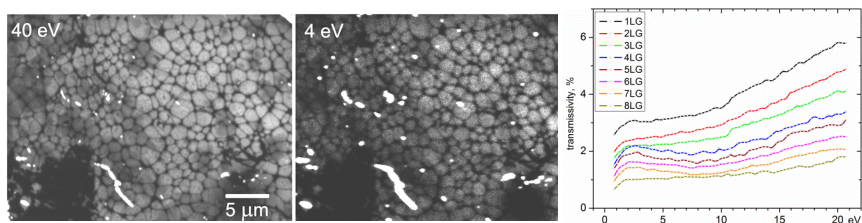


Figure 3 Micrographs of a 3 to 5 LG graphene sample taken in a UHV microscope (*left*); the measured energy dependence of transmissivity (*right*).

References:

- [1] Müllerová I. and Frank L., *Advances in Imaging and Electron Physics* **128** (2003) p. 309.
- [2] Frank L. and Mikmeková E., in these proceedings.
- [3] The authors acknowledge funding from the Technology Agency of the Czech Republic (Competence Centre Electron Microscopy, no: TE01020118) and from the MEYS of the Czech Republic (LO1212).

FABRICATION OF NANO-SLITS FOR A MONOCHROMATOR WITH DOUBLE OFFSET CYLINDRICAL LENSES

T. Ogawa^{1*}, GW. Gang¹, I.-Y. Park¹, JH. Kim¹, S.J. Ahn¹, and BL. Cho¹

¹Korea Research Institute of Standards and Science, 267 Gajeong-ro, 305-340, Daejeon, Rep. of Korea

*e-mail: togawa@kriss.re.kr

Various types of monochromators (MCs) have been proposed, evaluated, and commercialized for advanced charged particle beam apparatuses such as (S) TEMs and SEMs [1-3]. MCs improve spatial resolutions especially at low energy regimes and energy resolutions of EELS spectra. Both are achieved by narrowed energy spreads of electron beams. Recently, we have proposed a new MC with double offset cylindrical lenses (CLs) [4-6]. Its operation principle is similar with Möllenstedt energy analyzers [7]. As an initial stage of development, we've described optics of the MC with 1st order matrixes [4] and higher order aberrations [5] together with its performances. We've estimated improvements in SEM performance at low voltages with the MC [6]. Fig. 1 shows schematics of this MC.

For a MC, an energy resolution δ_k is given by an equation $\delta_k=2d_x/D_k$ with an energy dispersion D_k and a width d_x of an energy selection slit. The typical values of the energy dispersion D_k , which are determined by optics, are 5~50 $\mu\text{m}/\text{eV}$. To achieve an energy resolution of 10 meV, the slit width d_x of 200 nm is required for D_k of 40 $\mu\text{m}/\text{eV}$. In addition, these slits are needed to be high aspect ratio of d_y to d_x with a slit length d_y in the vertical direction. This is attributed to asymmetric optical paths of the MC for avoiding electron-electron interactions. Fig. 1 also represents schematics of the beam profiles and the nano-slit on the energy selection plane Z_2 .

These nano-slits are key components to realize the MC with high energy resolutions. Therefore, we execute a feasibility study on fabrication of the nano-slits. We adopt commercial Si_3N_4 thin films with thicknesses of 200 nm. Pt layers are deposited on both top and bottom surfaces of the films with a sputter coater in order to reduce electron penetration depth and prevent from charge accumulations. The thicknesses of the Pt layers are estimated to be 20 nm based on preliminary measurements of deposition rate with an AFM. Mook has utilized EB lithography and dry etch methods for slit fabrication [2]. Here, we adopt FIB etching methods due to its high flexibility. Based on the optical simulation [5], we specify five types of slits dimension and fabricate ten slits for each size with a FIB (Helios NanoLab, FEI). We evaluate these slits with a SEM (S5000, Hitachi) at an energy of 3 keV, which is equivalent to a pass energy of the MC. Fig. 2 shows SEM micrographs of a fabricated slit in two signal modes. The secondary electron image (SE) gives surface information of the slit. The scanning transmitted electron image (STEM) shows that this slit has an appropriate function as an obstacle to electron beams at 3 keV. The electron range simulation with Monte Carlo methods confirms this result. In addition, the STEM image gives actual sizes of the slit in similar operation conditions with the MC. The measured values of d_x and d_y are 172 nm and 9743 nm, respectively. The aspect ratio (d_y/d_x) of the slit is 56.

In conclusion, we conduct a feasibility study on nano-slits fabrication for the MC with double offset CLs. These slits can be applicable to various kinds of MCs and energy analyzers with high energy resolutions. The detailed discussion will be given in the conference.

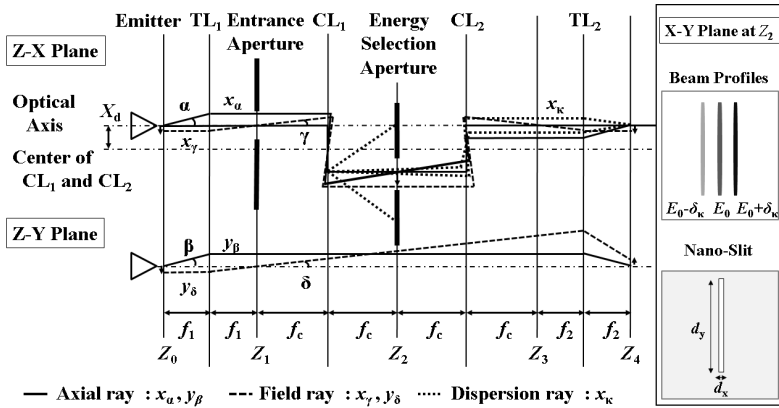


Figure 1 Schematics of the new MC. The configurations of two offset cylindrical lenses (CL₁ and CL₂), an emitter, transfer round lenses (TL₁ and TL₂), and apertures are shown. At the right side, schematics beam profiles and nano-slit on the energy selection plane (Z₂) are also shown.

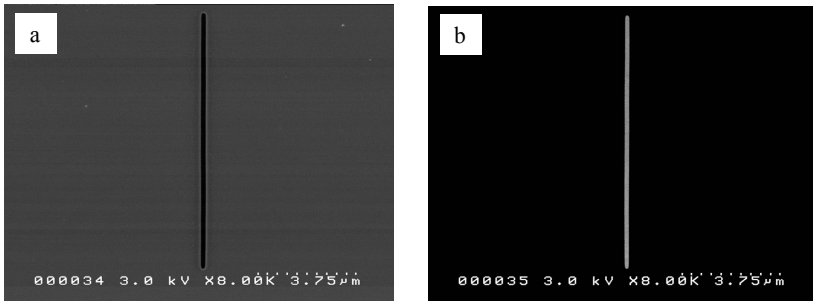


Figure 2 SEM micrographs of a fabricated nano-slit in a SE mode (a) and a STEM mode (b).

References:

- [1] H. Rose, *Ultramicroscopy* **78** (1999), p. 13-25.
- [2] H. M. Mook, P. Kruit, *Ultramicroscopy* **81** (2000), p. 129-139.
- [3] A. Henstra, et al, *Microsc. Microanal* **15 (Suppl 2)** (2009), p. 168-169.
- [4] T. Ogawa, B. Cho, *Nucl. Instrum. Methods. A* **772** (2015), p. 5-13.
- [5] T. Ogawa, B. Cho, *Nucl. Instrum. Methods. A* **800** (2015), p. 18-28.
- [6] T. Ogawa, et al, *J. Vac. Sci. Technol. B* **33 (6)** (2015), p. 06FJ01-1-11.
- [7] G. Möllenstedt, *Optik* **5** (1949), p. 499-517.
- [8] Grant number: CAP-14-3-KRISS.

OPTIMAL X-RAY DETECTION FOR THIN SAMPLES IN LOW-ENERGY STEM

J. Rozbořil¹, M. Oral^{1*} and T. Radlička¹

¹Institute of Scientific Instruments of the CAS, Královopolská 147, Brno, Czech Republic

*e-mail: oral@isibrno.cz

In many applications it is desirable to perform energy-dispersive X-ray spectroscopy (EDS) on very thin samples at low primary beam energies in a STEM. Thin samples, or lamellae, with the thickness of about 10 nm, are mostly prepared in focused ion beam instruments (FIBs), and they are used to evaluate experiments in the development of thin films and coatings, in the semiconductor industry, and in other applications. EDS then provides a map of different chemical elements or compounds in the sample, obtained by scanning the electron beam in a raster. Often the qualitative composition is known as a limited set of materials and only their distribution on the sample is to be determined. For large batches of samples fast measurements are desired to maximize utilization of expensive equipment. In this study we found a method to minimize the time needed to reliably acquire an elemental map by determining the optimal detector placement and the minimal necessary primary electron dose per pixel.

An advantage of thin samples is the small X-ray interaction volume. In the EDS setup with a bulk sample, the X-ray interaction volume size can be in the micrometre range. With thin samples in STEM, sub-nanometre resolution can be reached as it is limited largely by the probe size; and aberration correction is feasible even at low energies [1]. However, this is at the expense of the collected signal strength as the probability of a characteristic X-ray emission is rather low for an electron during the short travel through the sample. On the other hand, the emission of the unwanted bremsstrahlung which obscures the useful characteristic peaks is also decreased. Now the low energy (by the STEM standards, a few tens of keV) becomes beneficial, as the intensity of X-ray radiation tends to increase for lower energies, albeit again for both the characteristic radiation and the bremsstrahlung [2].

The SDD (silicon drift detector) is the most common detector type in EDS [3]. Its efficiency is given by the collection solid angle and the orientation with respect to the primary beam and the sample. While the characteristic X-ray intensity is isotropic, the bremsstrahlung is anisotropic along the direction of the beam [2]. The angular position of the detector can be optimized for the highest difference between the two types of X-rays, speeding up the measurement.

The method we developed makes use of reference X-ray spectra for the expected set of materials, simulated for the same conditions as in the analysis of an unknown sample, namely the specimen thickness, the direction of the primary beam, and the size and the position of the detector. Simulation allows to collect the characteristic and the bremsstrahlung parts separately. The influence of the detector on the collected signal is taken into account in the form of its “detector function”, the probability density in the *recorded* X-ray photon energy, which depends on the real *entrance* energy of the incoming photon [3].

When an actual spectrum is collected, it is matched against each reference spectrum by fitting a linear combination of the simulated characteristic and bremsstrahlung parts on it. A “goodness of fit” parameter is computed for each fit, $R_j = 1 - \frac{\sum_i (f_j(E_i) - I(E_i))^2}{\sum_i (f_j(E_i) - \bar{I})^2}$, where $f(E)$ is the j^{th} reference spectrum, $I(E)$ is the measured spectrum and \bar{I} is its average value. The parameter R ranges between zero, for no similarity, to one, for the complete agreement between the two spectra.

In practical measurements it is often safe to assume that a certain location on the thin sample contains just one from the set of expected materials, and that they mix just in thin boundaries. That simplifies further considerations (although the procedure can be generalized). The highest value of R on the set of the reference spectra is then obtained for the correct material. However, at low electron doses, the measured spectrum may be so poor that the identification is unreliable. As the dose is increased, the value of R will steadily increase for the correct material, but it will vary insignificantly for the other substances in the reference set.

We simulated the complete procedure for a beam perpendicular to a sample with the thickness of 10 nm. In pyPENELoPE [4, 5] we calculated accurate reference spectra using large electron doses. Then we also simulated the “measured” spectra with low electron doses. We studied dependences of the goodness of fit and other quantities on the electron dose and other parameters. We also repeated the simulation for different primary electron energies and different detector elevation angles that were assumed as mechanically feasible in an instrument. Fig. (a) shows that a dose of a few tens of millions of electrons already gives a fairly reliable material identification for any detector position. Fig. (b) confirms the expected higher time requirements at higher electron energies.

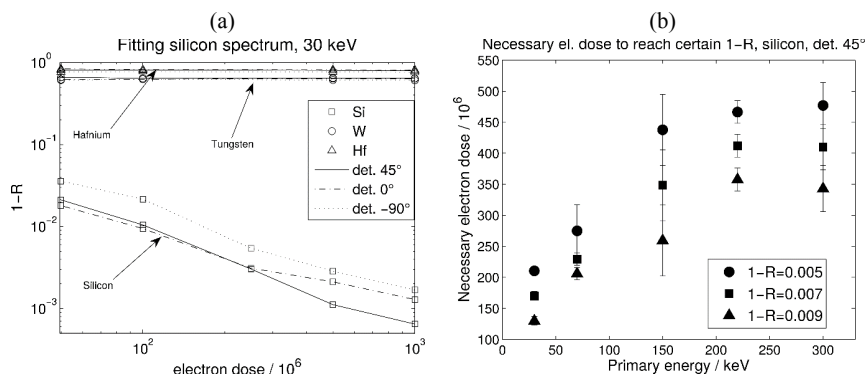


Figure (a) An example of the dependence of $1 - R$ (which is better suited for logarithmic plots than R) for a silicon sample matched against different reference spectra with the detector under different elevation angles relative to the sample plane (positive values are above the sample). **(b)** The required primary electron dose to reach reliable levels of agreement between the measured and the corresponding identified reference spectra (non-matching references usually give $1 - R < 0.4$). Note that the dose of 10^8 electrons is reached in 16 ms at the current of 1 nA.

References:

- [1] Kaiser U. et al., *Ultramicroscopy* **111** (2011), p. 1239-1246
- [2] Kissel L., Quarles C. A., Pratt R.H., *Atom. Data Nucl. Data* **28** (1983), p. 381—460
- [3] Hashimoto T. et al., *J. Phys* **312** (2011), section 5
- [4] pyPenelope online presentation, <http://pypenelope.sourceforge.net/>
- [5] Salvat F., Fernández-Vera J., Sempau J., *PENELOPE-2006: OECD/NEA Data Bank*. (2006)
- [6] Computational resources were provided by the CESNET LM2015042 and the CERIT scientific Cloud LM2015085 under the programme "Projects of Large Research, Development, and Innovations Infrastructures".

THE INFORMATION DEPTH OF BACKSCATTERED ELECTRON IMAGING

J. Piňos, Š. Mikmeková and L. Frank

Institute of Scientific Instruments of the CAS, v. v. i., Královopolská 147, 612 64 Brno, Czech Republic

*e-mail: pinos@isibrno.cz

Of the conventional imaging signals in the scanning electron microscope (SEM), the secondary electrons generally reflect surface properties of the sample, while the backscattered electrons (BSE) are capable of providing information about complex properties of the target down to a certain subsurface depth. Contrast mechanisms are combined according to the energy of incident electrons and energy and angular acceptance of BSE detection. In all cases, a question arises concerning the information depth of this mode. No applicable answer provides a definition declaring this depth as that from which we still obtain useful information about the object [1]. We can employ software simulating the electron scattering in solids, while experimental approaches are also possible. Moreover, two analytic formulas can be found in the literature [2,3] (with the mass thickness in eq. 2 transformed into the depth value):

$$R_{BSE} = \frac{7 A E^{1.67}}{\rho Z^{0.9}} \quad (1), \quad R_{BSE} = \frac{28 E^{1.54}}{\rho} \quad (2)$$

where R_{BSE} (nm) is the information depth of the BSE emission, A (g mol^{-1}) is the atomic weight, Z is the atomic number, E (keV) is the energy of incident electrons and ρ (g cm^{-3}) is the density of the target.

In order to simulate the scattering of electrons inside the material and identify those finally reflected as BSE, we can choose from several widely available programs treating the movement of electrons in a fully conductive amorphous target. We have used the CASINO program and its output “Z Max backscattered” which provides a histogram of maximal depths achieved by electrons finally backscattered. This plot peaks at the most probable depth from which the BSE come and one can establish a threshold for the information depth on the falling slope. We have tried to put this limit at the halved height of this peak (criterion I) and, in view of the significant difference from both calculated and measured depths, we took an optimum threshold that just 8.3 % of BSE exceed (criterion II) – see Fig. 3.

Measurement of the information depth requires confronting the plane view in the image signal under examination with independent depth information, best obtained from a cross-sectional view of the same scene. Optimum objects seem to be precipitates immersed in a matrix to suitable depths and providing sufficient mutual contrast; we have used copper precipitates growing in 18Cr-3.0Cu stainless steel (Fig. 1). In addition to massive appearance of tiny precipitates inside grains, large precipitates grow at the grain boundaries as the objects of choice for this purpose. In the plane BSE view, the size of the sharp contour of a precipitate varies with electron energy and when cutting a section across the precipitate, we can seek out the same dimension in the FIB (focused ion beam) prepared cross-sectional image and establish its depth below the target surface (Fig. 2). This procedure works down to a depth of the maximum dimension of the precipitate, i.e. along its convex upper part.

Fig. 3 shows that the information depth data calculated according to both above equations is extremely similar to each other and also fit the experimental data. The same holds true of the simulated depths if criterion II is chosen which does not otherwise follow from any other aspect of the scattering simulations. We have also built a distribution of tiny precipitate counts vs. electron energy that could, if spread homogeneously, also indicate the information depth. Fig. 3 shows this dependence differing drastically from all previous ones; it grows with depth much more slowly than expected, obviously due to the progressively broadening beam and hence decreasing contrast. However, our experimental data, together with calculated and simulated data, seems to confirm that eqs. (1) and (2) are useful for routine use.

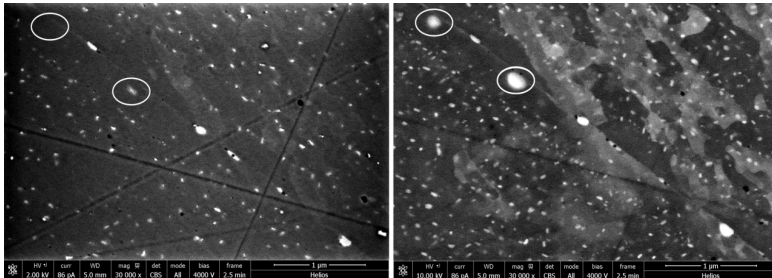


Figure 1 BSE micrographs taken at 2 keV (left) and 10 keV (right).

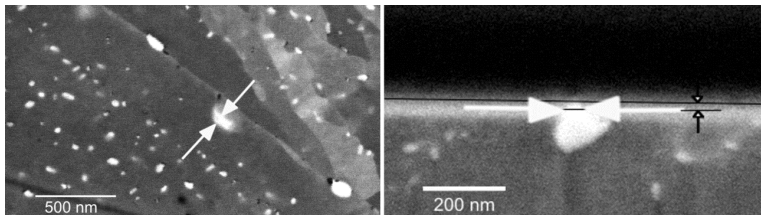


Figure 2 Scheme of evaluation of the information depth upon two views of an object.

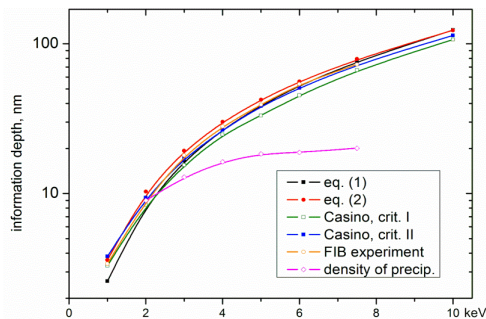


Figure 3 Comparison of measured, calculated and simulated information depths.

References

- [1] Powell C.J. et al., *J. of Surface Analysis* **17** (2011), p.170-176.
- [2] http://www.emal.engin.umich.edu/courses/sem_lecturecw/SEM_bse2.html
- [3] Reimer L., *Scanning electron microscopy*, Springer 1998, Sect. 4.1.2.

SCANNING VERY LOW ENERGY ELECTRON MICROSCOPY FOR THE CHARACTERIZATION OF POLYCRYSTALLINE METAL SAMPLES

Z. Pokorná*, A. Knápek

Institute of Scientific Instruments of the Czech Academy of Sciences v.v.i., Královopolská 147, 61264 Brno, Czech Republic

*e-mail: zuzana.pokorna@isibrno.cz

We explored the possibility of a Scanning Electron Microscopy technique for the determination of crystallographic orientation, based on the measurement of the reflectivity of very low energy electrons. Our experiments are based on the concept that in the incident electron energy range 0–30 eV, electron reflectivity can be correlated with the electronic structure of the material [1], which varies with the local crystallographic orientation of the specimen.

The motivation for the development of this technique was to achieve a quick and high-resolution means for determining the crystallographic orientation of very small grains (<1 μm) in a polycrystalline material. The key limiting factor was the cleanliness of the sample surface and also the geometrical setup of the experiment.

The experiment was performed in an Ultra High Vacuum Scanning Low Energy Electron Microscope (UHV SLEEM-III) of in-house design, equipped with a Cathode Lens assembly. This allows imaging at arbitrarily low incident electron energies (down to units of eV) without significant deterioration of resolution [2]. The samples, Al and Cu poly- and single crystals, were in situ cleaned in the Preparation Chamber of the UHV SLEEM-III by several cycles of Ar ion sputtering and heating to 450 °C.

They were then observed in the Main Chamber at a working pressure of $5 \cdot 10^{-8}$ Pa which ensures a very low rate of surface contamination. Series of images taken at incident electron energies between 0 and 30 eV with a step of 0.3 eV were taken. These were then processed to obtain the reflectivity curves [3].

Within the arrangement presented here we tested the ability to determine the local crystallographic orientation of grains in a polycrystalline sample from their very low energy electron reflectivity. Acquired data show that there is indeed an agreement which is however dependent also on the in-plane orientation of the grain. This is probably due to the strongly directional reflectivity distribution of the specimen – a result of diffraction and channeling effects – which also causes a portion of the signal to disappear in the central bore of the scintillation detector. This effect allows discerning between twin grains and is more pronounced in denser crystal faces. The state of the specimen surface, such as roughness or the presence of hydrocarbon adlayers and native oxide, is an influence on its own. Contribution of electron channelling effects is also discussed.

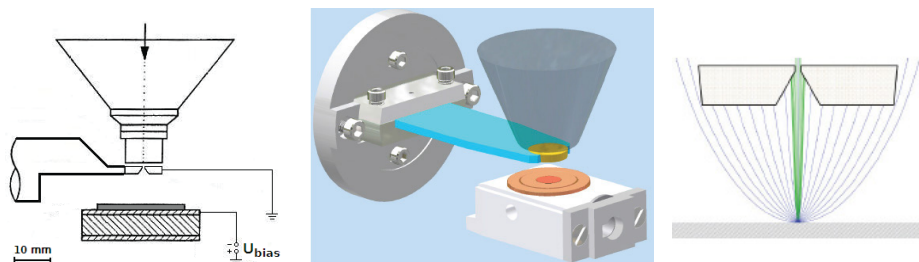


Figure 1 Schematic sketch (left) and a CAD model (center) of a Cathode Lens assembly [2]. Since no in-lens detection is used here, a part of the signal electron bunch leaves through the central bore and is lost for detection (right).

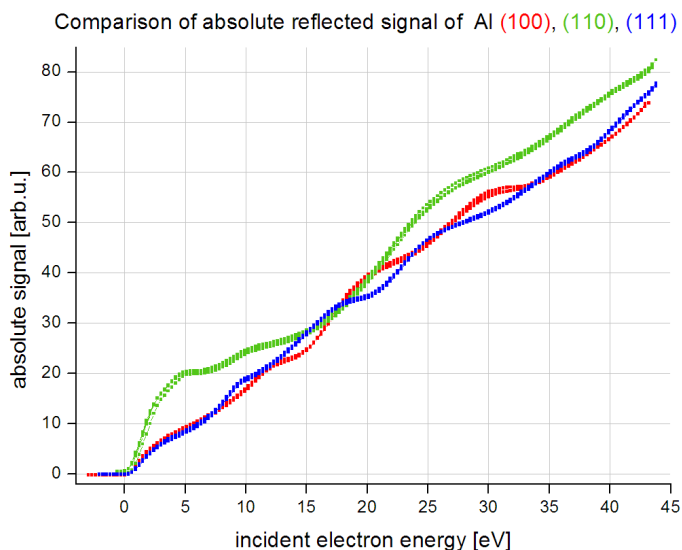


Figure 2 Experimental data curves.

References:

- [1] Bauer, E. „LEEM basics. Surface Review and Letters 5, no. 6 (1998): 1275–1286.
- [2] Müllerová, I. and Frank, L. „Scanning low-energy electron microscopy.“ Advances in imaging and electron physics vol. 128 (2003): 309–443.
- [3] Pokorná, Z., Mikmeková, Š., Müllerová, I. and Frank, L. „Characterization of the local crystallinity via reflectance of very slow electrons.“ Applied Physics Letters 100, no. 26 (2012): 261602–261602.

CORRECTION OF MISALIGNMENT ABERRATIONS OF A HEXAPOLE CORRECTOR USING THE DIFFERENTIAL ALGEBRA METHOD

T. Radlicka¹, M. Oral¹

¹ Institute of Scientific Instruments of the ASCR, v.v.i. Královopolská 147, 612 64, Brno, Czech Republic

*e-mail: radlicka@isibrno.cz

Overcoming the limitations of the Schertzer theorem is a long story in electron microscopy. Although the basic principle of a spherical aberration (C_3) correction was suggested as early as in 1947 [1] the first experimental correctors of spherical aberration were only realized in the last decade of the 20th century [2-4]. The recent multipole correctors are designed for high-energy TEM or STEM, where the corrector system enables reaching the atomic resolution. On the other hand, the corrector for low-energy SEM has been developed [5] but this type of corrector must also contain chromatic aberration (C_C) correction to reduce the effect of the non-zero energy width. Recently, the energies of SEM reach 30 keV and transmission mode (TSEM) is a standard part of the instrument. Standard resolution in TSEM is about 0.6 nm and it is limited by C_3 . Reaching atomic resolution with this set-up is not a real expectation because of its instability, but the resolution of about 0.2 nm would increase the field of applications. Corrector for these type of instruments should be (a) simple, compact and cheap (b) only spherical aberration of the third, optionally the fifth order must be corrected (c) effect of the chromatic aberration may be reduced by energy filtering. We studied design based on Rose's hexapole corrector [6].

The eikonal method is a standard tool for the calculation of the system aberration. However, our calculation is done using the differential algebra (DA) method to show the viability of the method in the design of the aberration corrected systems. The DA method is a very valuable tool for the calculation of aberrations in general electron or ion optical systems. It can be straightforwardly used to calculate high order aberration coefficients, which is limited only by the accuracy of the high order derivatives of the axial field. We used the procedures described in [7] to resolve that difficulty. Using the DA method, one finds the solution of the trajectory equation in the form of the polynomial in the position and slopes in the object plane and the energy deviation [8, 9],

$$\vec{q}(z) = \sum_{i_1, i_2, i_3, i_4, i_5} \vec{\xi}_{i_1, i_2, i_3, i_4, i_5}(z) x^{i_1} y^{i_2} x'^{i_3} y'^{i_4} dE^{i_5}$$

where $\vec{q} = (x, y)$ is a vector of the transversal coordinates and $\vec{\xi} = (\xi_x, \xi_y)$. When this form of the solution is substituted into the trajectory equation, the fields are also expressed in the form of the polynomials of the transverse coordinates and the both sides of the trajectory are expanded into a polynomial, a differential equation can be found for all the coefficients. When these equations are solved for the initial condition $\xi_{10000} = \xi_{01000} = \xi_{00100} = \xi_{00010} = \xi_{00001} = 1$ and 0 for all other coefficients, a solution is found.

Calculation of an ideal RHC using the DA method

The corrector will be applied to a highly optimized system with $C_3 = 0.88$ mm, $C_5 = 0.46$ mm, and $C_C = 1.7$ mm at the primary beam energy of 30 keV. With a sufficiently bright source the optimal probe size is 0.35 nm for the beam energy width of 0.6 eV, which can be improved to

0.18 nm with the ideal C3 corrector. When the energy filter is used, the resolution can reach 0.1 nm for the energy width of 0.1 eV without significant probe current decrease (the loss of the electrons by the energy filtering is compensated by an increase of the optimal aperture angle). This resolution is beyond reasonable value for the standard SEM, because of instrument instabilities.

The principle of the Rose hexapole corrector has been described in many publications [10]. It is a double symmetrical system consisting of two hexapoles and a 4f doublet lens between them. The center of the first hexapole coincides with the object focal plane of the doublet and the center of the second one coincides with the image focal plane of the doublet. This configuration guarantees that up to the third order the corrector behaves like a lens with negligible spherical aberration.

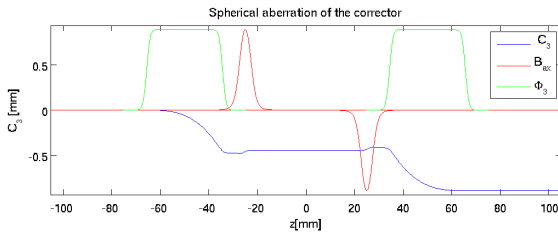


Figure 1 Properties of the analyzed Hexapole corrector of the spherical aberration.

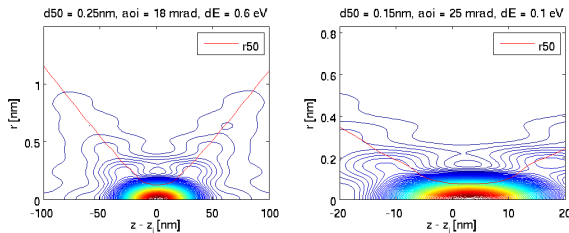


Figure 2 Beam profiles for the optimal aperture in the system corrected for both C_3 a C_5 .

The result of the DA calculation is a set of coefficients $\xi_{i_1, i_2, i_3, i_4, i_5}(z)$ which is not a common representation for the aberrations which can be obtained by transitioning to the complex coordinates $w = x + i y$ and by using a parametrization by the image paraxial coordinates:

$$w(z) = \sum_{i_1, i_2, i_3, i_4, i_5} u_{i_1, i_2, i_3, i_4, i_5}(z) \alpha^{i_1} \bar{\alpha}^{i_2} \gamma^{i_3} \bar{\gamma}^{i_4} dE^{i_5}$$

where $\alpha = x'_i + i y'_i$ is the paraxial slope in the image and $\gamma = x_i + i y_i$ is the paraxial position in the object. Moreover, from the aberration theory it is known that each coefficient

$u_{i_1, i_2, i_3, i_4, i_5}(z)$ describes object and slope coefficient in the case of the axially symmetrical paraxial approximation:

$$u_{i_1, i_2, i_3, i_4, i_5}(z) = u_\gamma(z)C_{i_1, i_2, i_3, i_4, i_5}(z) + u_\alpha(z)C_{i_1, i_2, i_3, i_4, i_5}(z)$$

$$u'_{i_1, i_2, i_3, i_4, i_5}(z) = u'_\gamma(z)C_{i_1, i_2, i_3, i_4, i_5}(z) + u'_\alpha(z)C_{i_1, i_2, i_3, i_4, i_5}(z)$$

with u_α being the axial fundamental ray ($u_\alpha(z_i) = 0, u'_\alpha(z_i) = 1$) and u_γ the off-axial fundamental ray ($u_\gamma(z_i) = 1, u'_\gamma(z_i) = 0$). This is equivalent to the transition to the interaction coordinates in the Lie algebra method [9]. Calculation of the object and gradient coefficients can be done very simply by solving previous equations for all the coefficients $u_{i_1, i_2, i_3, i_4, i_5}(z)$

A calculation of the basic properties of the Rose Hexapole corrector is shown in Fig. 1. It was set to correct the spherical aberration of the objective lens. Fig. 2 shows the longitudinal beam profiles in the vicinity of the image plane for the optimal aperture. The first case is for the beam without energy filtering, the second one is for the energy-filtered beam with the energy width of 0.1 eV. The increase of the optimal resolution to 0.15 nm is given due to an increase of C_c in the doublet lens and a change of the objective lens properties (an additional transfer lens between the corrector and the objective lens was placed to correct C_5).

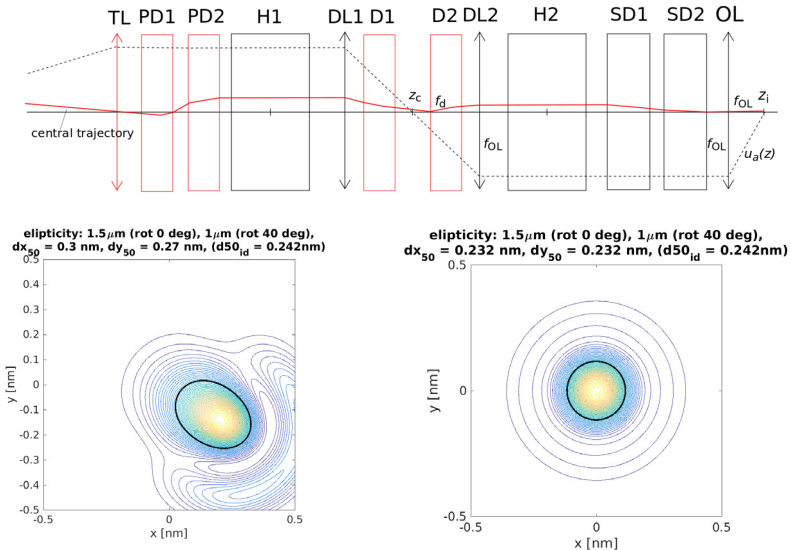


Figure 3 A system with correcting elements and the effect of the misalignment aberrations on the spot size. Ellipticity 1.5 μm(0 deg) and 1μm(40 deg).

Misalignment aberrations of the C3 corrected system.

The system contains very strong elements, the two hexapoles that have second-order aberrations. The double symmetry of the system, using the second hexapole, serves to correct the second order effect of the first hexapole. The result of such a setting is that the optical properties are very

sensitive to the asymmetry of the system, misalignment aberrations and system imperfections. If the system is not properly corrected, its resolution can be even worse than that of the uncorrected one. Some of the imperfections can be compensated with no additional elements, but for some of them an addition of auxiliary correction elements is necessary.

The effect of the asymmetry of the doublet lens and the hexapoles can be compensated by the independent excitation of the doublet lenses and both hexapoles, required accuracy have to about 10^{-6} . However, for compensation of off-axial position of the hexapoles and ellipticity of doublet lens the additional correcting elements are necessary. An off-axial position of the first hexapole must be compensated by a double deflection system in front of the corrector and an off-axial position of the second hexapole by another double deflection system between the lenses of doublet. The both deflection systems make the central trajectory to coincide with the hexapole axis. Ellipticities of the doublet lenses generate additional quadrupole fields that result in two-fold astigmatism. It can be compensated by a standard double stigmator system in front of the objective lens. However, the effect of the weak parasitic quadrupole field is combined with the effect of the second hexapole which leads to a nonzero second order axial coma B_2 and four-fold astigmatism A_3 . These effects can be compensated by a slightly off-axial position of the beam in the hexapoles, which can be controlled by the double deflection systems. The off-axial position of the central trajectory in the hexapoles generates weak quadrupole field which can compensate the effect of the doublet lens ellipticities.

The optimization of the corrector using the DA method is hindered by the fact that the method does not provide explicit formulas for the aberrations coefficients, only their values for a given position along the optical axis. The optimization is then carried out using the standard simplex minimization method, where the minimized function is $B_2^2 + A_3^2$, for results see Fig. 3. In the case of the ellipticity four parameters were found, which took about one hour. This approach mimics closely to the experimental procedure for system alignment in which aberration measurement is replaced with numerical calculation.

References:

- [1] O. Scherzer, *Optik* **2** (1947), p. 114-132.
- [2] J. Zach and M. Haider, *Optik* **99** (1998), p. 112-118.
- [3] M. Haider, S. Uhlemann, et al, *Nature* **392** (1998), p. 768-769.
- [4] O.L. Krivanek, N. Dellby & A.R. Lupini, *Ultramicroscopy* **78** (1999) 1-11.
- [5] Zach, J. & Haider, M., *Nucl. Inst. Methods Phys. Res. A* **363** (1995), p. 316-325.
- [6] Rose, H., *Nucl. Instruments Methods* **187** (1981), p. 187-199.
- [7] T. Radlička, B. Lencová, *Ultramicroscopy*, **110**(9), (2010), p. 1198-1204.
- [8] M. Berz, *Adv. Imaging. Elect. Ph.* **108** (1999).
- [9] T. Radlička, *Adv. Imaging. Elect. Ph.* **151** (2008), p. 241-362.
- [10] M. Haider, H. Muller, S. Uhlemann, *Adv. Imaging Electron Phys.* **153** (2008), p. 43-119.
- [11] The work was supported by MEYS CR (LO1212, 7H13015) together with EC (ALISI No. CZ.1.05/2.1.00/01.0017) and by ENIAC JU (E450EDL No. 325613)

DEVELOPMENT OF THE NANO APERTURE ION SOURCE (NAIS)

L. van Kouwen, D. Radovanović and P. Kruit

Delft University of Technology – Department of Imaging Physics, Delft, Netherlands

*e-mail: d.radovanovic@tudelft.nl

Focused ion beams are irreplaceable in nano-fabrication and ion microscopy. The development of a high-brightness He^+ source had great impact since it helped to overcome the limitations of Ga^+ beams. Further advances can be achieved by developing a source capable of using a broad range of different gaseous species. Our approach is to use electron impact ionisation in gas confined in a small space between two thin membranes.

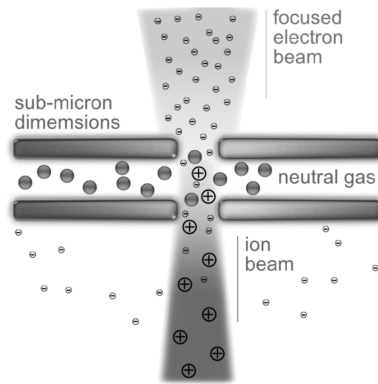


Figure 1 The essence of the NAIS concept is focusing an electron beam onto a neutral gas to generate ions by electron-impact ionization. A high pressure is maintained by confining the gas between thin membranes. Extraction of ions is enhanced by an electric field between the membranes.

Theoretical analysis [1] predicts a brightness comparable, or even higher than that of Ga^+ sources. This is achieved by the small ionisation volume and the high electron current density. A short distance (~ 250 nm) between the membranes gives efficient ion extraction at low voltages across the membranes (sub-1eV) which, in turn, results in low energy spread. In a proof-of-concept experiment, ion beams of several gaseous species were created and measured for different pressures [1].

Recent experimental results with argon ion beams are shown in figure 2 and 3. Our current efforts are aimed at measuring the brightness using a knife-edge. We use a custom-made optical column that fits inside the chamber of an electron microscope. Small aperture size (~ 150 nm) ensures that the vacuum inside the microscope chamber is not compromised even for higher pressure of gas between the membranes. Electronics allows us to scan the ion beam over the sample and make transmission images (figure 3). We use a 1keV, 100nA electron beam to make Ar^+ ions. Although it is not the most efficient energy for ionising argon (Figure 2), a compromise had to be made since a beam of lower energy would be difficult to focus. The gas feed is equipped with a pressure controller such that the pressure can be changed in a

range from 60 mbar to 6 bar. Extraction of ions is enhanced by applying a bias voltage between the membranes of the chip. Current work is aimed at improving the setup in terms of signal stability, detector uniformity and chip alignment in order to achieve reliable measurements.

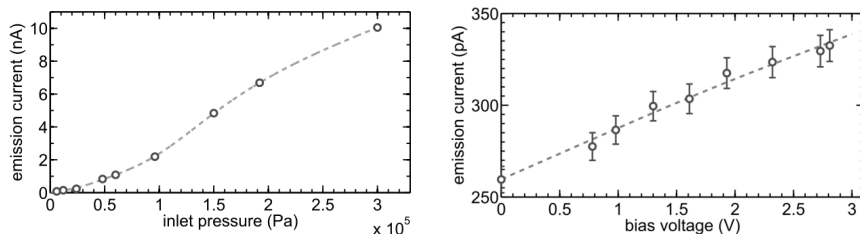


Figure 2 Recent argon ion emission current measurements. We control the total emission current by varying the pressure between the double membranes (left) and by changing the voltage across the membranes (right).

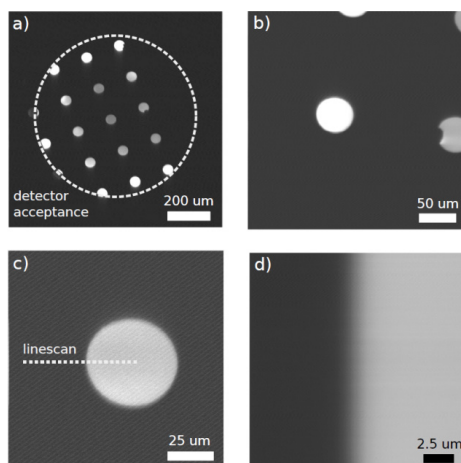


Figure 3 a) Wide field of view Ar⁺ ion image of sample (Si plate with 50µm holes). b) Individual hole. c) Direction of line scan for knife edge measurement. d) Image over scan

References:

- [1] D. Jun, V. G. Kutchoukov, P. Kruit, *J. Vac. Sci. Technol. B* **29**, 06F603 (2011).
- [2] Atomic and molecular collisions group, Rice university
www.ruf.rice.edu/~tmol/electron_data.html

This research is supported by FOM (Stichting voor Fundamenteel onderzoek der Materie) which is financially supported by NWO (Nederlandse Organisatie voor Wetenschappelijk Onderzoek) and FEI company. We would like to thank Aurelien Botman for his assistance and advice during the experimental work.

DIFFRACTION IN A SCANNING ELECTRON MICROSCOPE

T. Řiháček¹*, F. Mika¹, M. Matějka¹, S. Krátký¹ and I. Müllerová¹

¹Institute of Scientific Instruments of the CAS, v. v. i., Královopolská 147, 612 64, Brno, Czech Republic

*e-mail: rihacek@isibrno.cz

Manipulation with the primary beam phase in a transmission electron microscope (TEM) or a scanning transmission electron microscope (STEM) has drawn significant attention in the microscopy community in the recent years. Although a few applications were found long before, some are still subjects of a future research [1]. One of them is the use of electron vortex beams, which has very promising potential. It ranges from probing magnetic materials and manipulating with nanoparticles to spin polarization of a beam in an electron microscope.

The methods for producing electron vortex beams have undergone a lot of development in recent years as well. The most versatile way is holographic reconstruction using computer-generated holograms modifying either phase [2] or amplitude [3]. As the method is based on diffraction, beam coherence is a very important parameter here. It is usually performed in TEM at energies of about 100 – 300 keV which are well suited for diffraction on artificial structures for two reasons. The coherence of the primary beam is often reasonable, and the diffraction pattern is easily observed. This is however not the case for a standard scanning electron microscope (SEM) with typical energy up to 30 keV.

To find out whether SEM offers a possibility to perform such diffraction experiments, we used an experimental setup (Fig. 1) similar to that used in [4], which was implemented in the SEM FEI Magellan 400. The diffraction of the primary beam took place on a grating placed below the objective lens pole-piece. The diffraction pattern visualization is then achieved by scanning the diffracted beam across the contrasting vertical stripe placed in the specimen plane. As we needed the grating to be translationally invariant, we opted for a rectangular structure. This free-standing grating (Fig. 2) with a periodicity of 300 nm was fabricated from a thin silicon nitride membrane by a process developed by our team specifically for this instance. The process comprised of high-resolution electron lithography, reactive ion etching, platinum coating and other techniques. Electron lithography was also used to prepare the above mentioned contrasting stripes with a width of 0.25 – 4 μm .

To calculate the diffraction pattern a point source was considered emitting a spherical wave limited by a Gaussian-like aperture function. The wave passes through a thin objective lens, then the diffraction grating and finally it reaches the specimen plane. A paraxial approximation and Fresnel propagation of a wave was assumed, and both chromatic and spherical aberrations, as well as finite source size were taken into account.

Comparing the experimental and calculated data (Fig. 3) it can be seen that the diffraction patterns with clear intensity minima approximately fit the model in terms of visibility of fringes. The incoherent contributions cannot be observed at this scale since they have rather weak effect and influence only the structure of the individual peaks (Fig. 4).

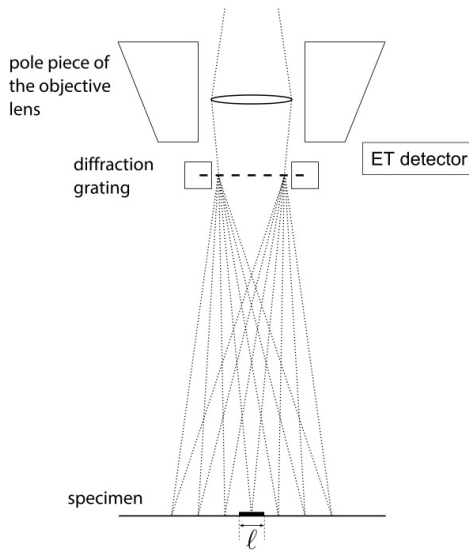


Figure 1 Experimental setup.

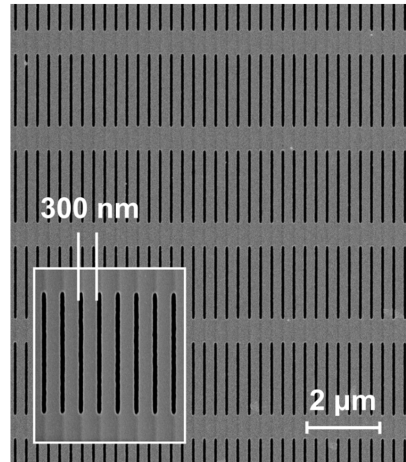


Figure 2 Diffraction grating.

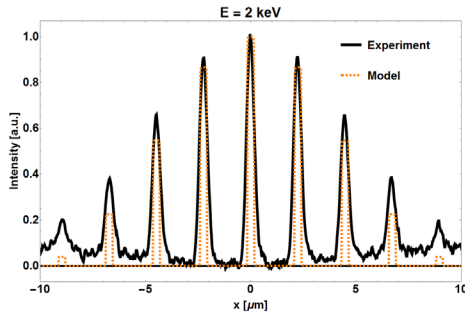


Figure 3 Diffraction pattern for the energy of 2 keV.

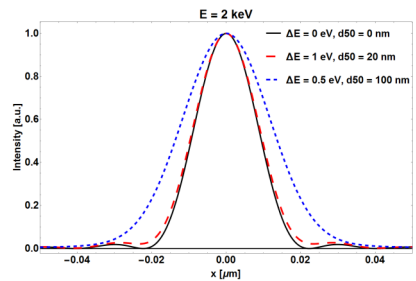


Figure 4 The effect of chromatic aberration and finite source size on the central peak.

References:

- [1] Guzzinati G. et al., *Ultramicroscopy* **151** (2015), p. 85 – 93.
- [2] Grillo V. et al., *Appl. Phys. Lett* **104** (2014), p. 043109.
- [3] Verbeeck J. et al., *Nature* **467** (2010), p. 301 – 304.
- [4] McMorran B. et al, *Ultramicroscopy* **106** (2006), p. 356 – 364.
- [5] The work is supported by the TA CR (TE01020118), MEYS CR (LO1212), its infrastructure by MEYS CR and EC (CZ.1.05/2.1.00/01.0017) and by CAS (RVO:68081731).
- [6] We thank Michal Lenc for valuable discussions and support.

SECONDARY ELECTRON SPECTROSCOPY AND ENERGY SELECTIVE IMAGING FOR THE ENGINEERING OF CARBON BASED MATERIALS

C. Rodenburg^{1*}, R. Masters¹, D. Lidzey², M. Uncovsky³, T. Vystavel³, F. Mika⁴

¹University of Sheffield, Materials Science & Engineering, Mappin Street, S13DJ, Sheffield, UK

²University of Sheffield, Physics & Astronomy, Hounsfield Road, S3 7RH, Sheffield, UK

³FEI Company, Vlastimila Pecha 1282/12, 627 00 Brno, Czech Republic

⁴Institute of Scientific Instruments, Královopolská 147, Brno, CAS, Czech Republic.

*e-mail: c.rodenburg@shef.ac.uk

That the fine structure of secondary electron emission spectra (SES) from carbon fibres is effected by fibre crystallinity and molecular orientation and linked to engineering materials properties such as modulus [1] was reported over three decades ago. In spite of this longstanding knowledge SES are not yet widely exploited for materials engineering of carbon based materials, probably due to a lack of instrumentation that is suitable to collect SES from beam sensitive materials and also has the capability to visualise, local variation based on SES shape. Thanks to rapid advances in low voltage SEM that offer energy selective imaging, it was recently demonstrated that differences in SES for different carbon based materials can be used to map chemical variations with sub-nanometer resolution [2] when only SE $8 < eV$ were selected to form the SEM images. Such high resolution is not surprising as the implementation of energy filtering in SEMs to improve image resolutions was previously advocated [3]. To fully exploit energy selective imaging for materials engineering the nature of the features in the SES must be determined.

Here we report a number of SES collected under standard SEM vacuum conditions at low primary beam energies (200eV-1keV) of materials with varying degree of sp² hybridisation, namely PCBM70 (a fullerene derivative) and P3HT a semiconducting, semi-crystalline polymer. Fig. 1a shows on the example of PCBM70 that the peak position of spectral features is reproducible and not solely a reflection of surface contamination. Multiple peaks are present in the SES, showing some similarity to SES in graphite [1, 4] where a 3 eV peak is reported to be linked to molecular orientation. Fig. 1b show SES of P3HT, which was spin cast from a chlorobenzene solution on to silicon substrates. SES collected at 200eV is relatively featureless while increasing the energy to 700 eV leads to a substantial additional peaks at 3eV and a smaller peak at 5eV. However, it leads to some charging as evident by the shift of the SES. When this shift is corrected (Fig 1d) peaks are found in the 1keV SES at the same energies. The SES collected with a 350eV primary beam does not have such clear peaks but some broad region of increased SE emission at 2.5-3.5eV and around 5 eV. Based on this we assume that the extra features are linked to inner shell excitations of carbon atoms. It is known that the processing of P3HT films effects the predominate molecular orientation. Therefore, Fig 1c contains spectra from P3HT films that were processed differently. Using chlorobenzene (CB) as solvent films cast on silicon are reported to result in mainly face on orientation which can be changed to edge on orientation by annealing [5]. Films cast from solution of Dichlorobenzene (DB) are reported to result mainly in edge on orientation [6]. Based on this we speculate that the strong peak at 3eV indicates the presence of face on P3HT as it is absent in SES the annealed CB film, or when cast from DBC. Therefore, images of annealed P3HT without (Fig 2a) and with energy selection SE (Fig 2b) are presented, only the latter revealing local misorientation based on the above discussion. Thus we suggest that SES in combination with energy selective imaging as a useful tool for optimising OPV active layer processing.

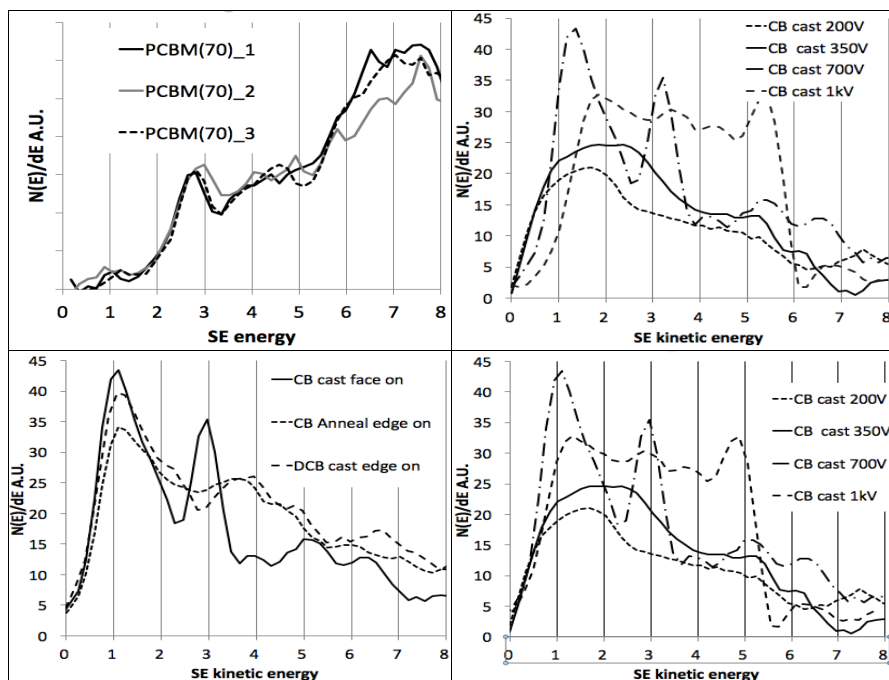


Figure 1 (a) SES of PCBM (1kV); (b) SES of P3HT using different acceleration voltages; (c) SES of P3HT with suspected different molecular orientations collected at 700V; (d) as (b) shifted to match onset.

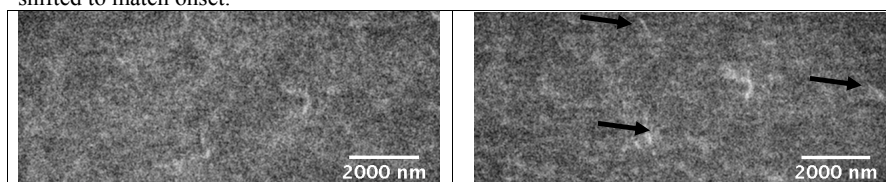


Figure 2 SEM images of P3HT cast from CB and annealed: (a) standard SEM; (b) Energy selective SEM. Bright features are could indicate remanent face-on orientation (see arrows).

References:

- [1] Willis R. F., Fitton B., and Skinner D. K., *Journal of Applied Physics* **43** (1972), p. 4412
- [2] Masters R. C. et al., *Nature Communications* **6** (2015) 6928
- [3] Griffin B. J., *Scanning* **32** (2011), p. 162-173
- [4] Papagno L. et al, *Physical Review B* **26** (4) (1982) p. 2320-2322
- [5] Park, Y. D. et al, *Electrochemical and Solid State Letters* **9** (11) (2006) G317-G319
- [6] Chu Chi-Wei et al, *Applied Physiscs Letters* **92** (2008) 103306
- [7] C. Rodenburg thanks EPSRC for support under grant EP/N008065/1

OPTICAL ARRANGEMENTS FOR PHASE-SENSITIVE IMAGING USING ELECTRON PTYCHOGRAPHY

J.M. Rodenburg*, S.Cao, and A.M. Maiden

Department of Electronic and Electrical Engineering, University of Sheffield, Mappin Street, Sheffield S1 3JD, UKstitution 1, Street, Postcode, City, Country

*e-mail: J.M.Rodenburg@shef.ac.uk

We describe the advantages and disadvantages of three optical configurations for undertaking electron ptychography. Ptychography is now a very well established technique in X-ray imaging [1], but adoption at electron wavelengths has been slow due to various experimental difficulties. The method relies on processing a series of 2D diffraction patterns collected in transmission from a set of 2D illumination positions. Each illumination area must overlap significantly with adjacent areas, so that the same information about the object is encoded in a number of diffraction patterns. This diversity allows fast and effective recovery of the phase and amplitude of the transmission function of the specimen, and also the illumination function, which may be highly-aberrated. The two key advantages of the technique are that the resolution of the reconstruction can be many times better than that of lens employed to create the illumination, and that the phase of the transmitted wave can be very strong (many phase wraps) unlike, say, the bright field image that relies on the weak phase approximation.

An important application is the ability to convert an ordinary SEM, with a modest resolution and stability envelope (say giving a resolution of 1.2nm), into a high-performance TEM simply by mounting a 2D detector below a transmission specimen (Figure 1a). Our latest results, refined by removing partial coherence effects, suggest that 0.14nm resolution can be achieved (Figure 1b), even at only 30keV (data from [2]). However, this configuration has limitations associated with the maximum field of view achievable: ironically, it can only work at high resolution because of the limited distance from specimen to detector, and the related sampling condition that arises. An entirely new form of electron ptychography very recently reported (see Figure 2a), which relies on moving an image across a selected area aperture in TEM, can obtain very good phase sensitivity over very large fields of view, and should in theory compete with all forms of electron holography [3]. A weak-phase approximation method for ptychography [4] has recently been re-implemented [5], but this has the disadvantage of requiring a very fast detector and the accumulation of tens of Gigabytes of data for each image reconstruction.

The question is: what is the best way of implementing electron ptychography? Competing parameters include the requisite degree of spatial coherence for a particular experimental set up, minimisation of electron dose, detector characteristics and the constraints of the electron optics employed. Our long-term objective is to implement electron ptycho-tomography at atomic resolution – plotting the coordinates of, say, 10^5 atoms within an entirely amorphous material. The key benefit of ptychography in this context is the sensitivity and linearity of the phase signal (proportional to the integrated atomic potential along the line of sight). An SEM-based system with a long working-length objective that allows for in-situ FIB would be desirable, although this is not ideal optics for ptychography *per se*.

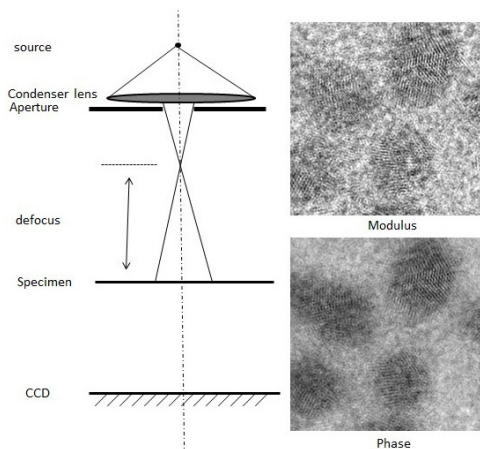


Figure 1 SEM configuration – note atomic columns visible in gold particles on amorphous carbon - the beam is scanned as diffraction patterns are recorded.

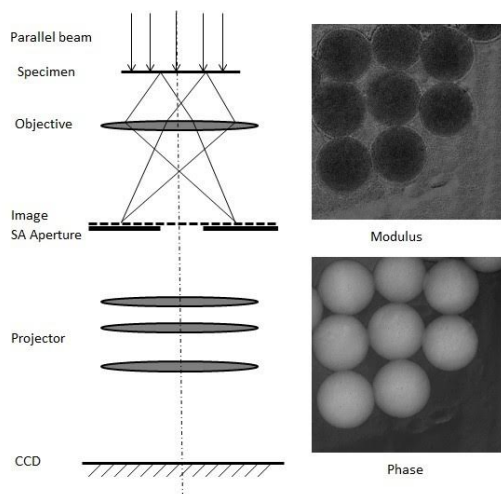


Figure 2 Selected area diffraction ptychography (SAP) can reconstruct very strong phase. The specimen is moved laterally as diffraction patterns are recorded.

References:

- [1] Thibault P, Guizar-Sicairos M and Menzel A J., *Synchrotron Radiat.* **21** (2014) p.1011-8
 - [2] Humphrey M., et al. *Nature Communications* **3** (2012) Art. No. 730
 - [3] Maiden A.M., et al. *Scientific Reports* **5** (2015) Art. No. 14690
 - [4] Rodenburg J.M., McCallum B.C and Nellist P.D., *Ultramicroscopy* **48** (1992) p. 304-314
 - [5] Pennycook T.J, et al., *Ultramicroscopy* **151** (2015) 160-167
- S.C Acknowledges financial support from Phase Focus Ltd.

EFFICIENT LINEAR PHASE CONTRAST AND OPTICAL SECTIONING IN THE ABERRATION-CORRECTED SCANNING TRANSMISSION ELECTRON MICROSCOPE

H. Rose and C. Ophus*

Ulm University, Albert-Einstein-Allee 11, 89069 Ulm, Germany

*Lawrence Berkeley National Laboratory, Berkeley, CA, USA

Improved correctors enable nowadays usable apertures up to 70mrad resulting in a resolution limit of 16λ which is about six times smaller than that of uncorrected electron lenses [1]. This possibility has significantly improved quantitative structural analysis in both TEM and STEM to sub-Å resolution and single picometer precision in materials science where many materials can tolerate very high electron doses. Compared to STEM, TEM phase contrast imaging is overwhelmingly preferred by the biological community because it provides an efficient means of imaging weak phase objects at doses at or below $10e/\text{Å}^2$. Resolution for biological materials is limited by the achievable signal-to-noise ratio (SNR) before the target structure is damaged or destroyed. In order to achieve maximum specimen resolution in the image of such objects as many scattered electrons as possible must be utilized for the image formation. The STEM operates usually in the dark-field mode with a detector collecting a distinct fraction of the electrons which are scattered out of the cone illumination cone. However, this fraction decreases with increasing resolution because the cone angle also increases. Therefore, methods are required which enable the use of the elastically scattered electrons within the cone of the non-scattered electrons beneath the object. Large aperture angles enable effective optical sectioning by means of “*holographic*” phase-contrast imaging in STEM which produces almost ideal linear phase-contrast images over a wide range of spatial frequencies with very high efficiency and could potentially be used to image soft matter and beam-sensitive samples. This imaging mode requires a high-speed segmented or pixilated bright-field detector and a Fresnel phase plate which can be formed with a sufficient degree of accuracy (a) by adjusting appropriately the coefficients $C_n, n \geq 3$ of the correctable spherical aberrations and the defocus $\Delta f = C_1$ of the objective lens [2] or (b) by a patterned SiN membrane together with $C_n = 0, n \geq 1$ [3], as shown schematically in Fig. 1.

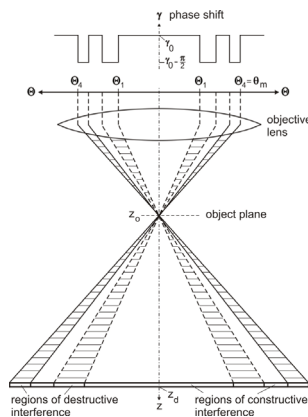


Figure 1 Fresnel phase plate yielding conical regions of constructive and destructive interference of the scattered wave with the non-scattered wave behind the object

In order to obtain highest efficiency the areas of the odd Fresnel zones must coincide with those of the even zones. By subtracting the signals of the detector segments covering the region of destructive interference of the scattered wave with the non-scattered wave from the signal recorded by the annular segments covering the regions of constructive interference, we obtain an efficient linear phase contrast image which represents a holographic image because the terms of the intensity which depend quadratic on the scattering amplitude cancel out. We demonstrate this behavior by the experimental results shown in Fig. 2 which simultaneously image the atomic-scale structure of weakly-scattering amorphous carbon and strongly-scattering gold nanoparticles. The image shows strong linear phase contrast for both materials, making the method a promising candidate for structural determination of soft matter and heterogeneous soft/hard matter samples even at low electron doses. The method is comparable to traditional phase contrast transmission electron microscopy and has the advantage to transfer the high and the low spatial frequencies, thus avoiding the low-spatial-frequency gap which poses a severe shortcoming of the TEM for imaging large details of biological objects with sufficient contrast.

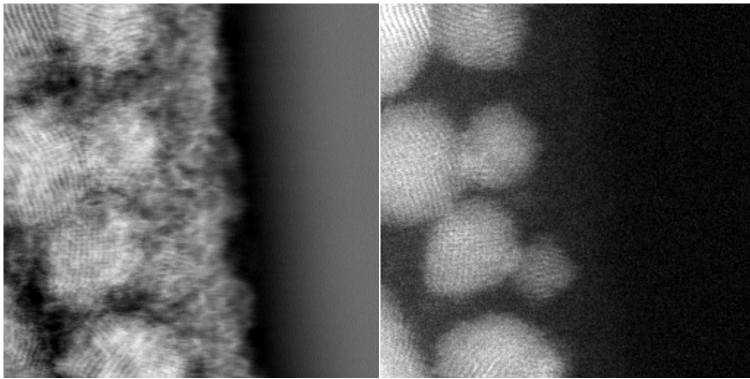


Figure 2 MIDI-STEM experiment of a heterogeneous sample. Images of gold NPs on a thin carbon support (left) using the pixelated bright-field detector and (right) the annular dark-field (ADF) detector.

The ADF image shows strong contrast for the gold nano-particles. The atomic planes are visible with the (111) plane spacing. The carbon support is very faintly visible in the ADF image, and though it can be distinguished from vacuum, but no structural information can be obtained. The phase-contrast image shown in Fig. 2 (left) also shows good contrast with a similar SNR for the atomic planes as the ADF image in Fig. 2 (right). However, contrary to the ADF image, the phase-contrast STEM image shows very strong contrast for the carbon support, especially at the vacuum edge.

Only atoms which are located within the depth of view $d_v = \lambda/\pi\theta_i^2$ are imaged with maximum resolution and contrast, where θ_i denotes the angle of the illumination cone. Since the image is entirely formed by the interference of the scattered wave with the non-scattered wave the image contrast of atoms not located within the depth of view is strongly suppressed. Owing to this behavior, holographic STEM imaging enables optical sectioning. Image simulations demonstrate that the method can be also be employed for thin crystalline objects.

References:

- [1] SALVE report Dec. 2015, unpublished
- [2] H. Rose, Phase Contrast in the Scanning Transmission Electron Microscope, *Optik* 39, 416 (1974).
- [3] C. Ophus et al. Efficient linear phase contrast in scanning transmission electron microscopy with matched illumination and detector interferometry. *Ncomms*10719, 2016

GOLDEN NANOPARTICLE IN OPTICAL TWEEZERS: INFLUENCE OF SHAPE AND ORIENTATION ON OPTICAL TRAPPING

M. Siler^{1*}, O. Brzobohaty¹, L. Chvatal¹, V. Karasek¹, A. Patak¹, Z. Pokorna¹, F. Mika¹ and P. Zemanek¹

¹ Institute of Scientific Instruments of the CAS, v.v.i., Kralovopolska 147, 61264 Brno, Czech Republic

*e-mail: siler@isibrno.cz

Noble metal nanoparticles (NPs) have attracted increased attention in recent years due to various applications of resonant collective oscillations of free electrons excited with light (*plasmon resonance*). In contrast to bulk metal materials, where this plasmon resonance frequency depends only on the free electron number density, the optical response of gold and silver NPs can be tuned over the visible and near-infrared spectral region by the size and shape of the NP. Precise and remote placement and orientation of NPs inside cells or tissue would provide another degree of control for these applications. A single focused laser beam – optical tweezers – represents the most frequently used arrangement which provides three-dimensional (3D) contact-less manipulation with dielectric objects or living cells ranging in size from tens of nanometers to tens of micrometers. It was believed that larger metal NPs behave as tiny mirrors that are pushed by the light beam radiative force along the direction of beam propagation, without a chance to be confined. However, recently several groups have reported successful optical trapping of gold and silver particles as large as 250 nm [1]. We offer an explanation based on the fact that metal nanoparticles naturally occur in various non-spherical shapes, see figure 1, and their optical properties differ significantly due to changes in localized plasmon excitation.

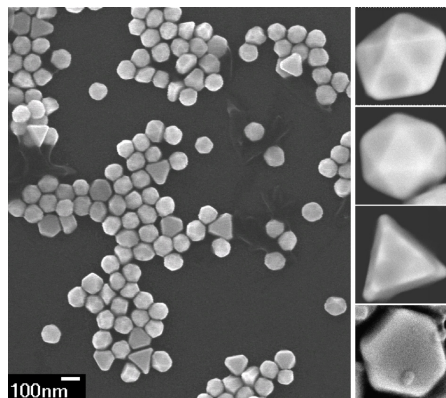


Figure 1 Gold NPs (diameter 100 nm British Biocell) observed by scanning electron microscope (FEI Magellan 400). Right-hand column shows detailed images of various particle shapes: decahedron, icosahedron, triangular and hexagonal prisms.

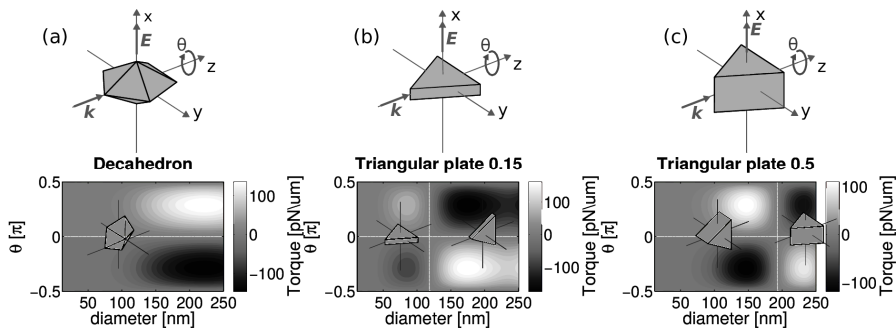


Figure 2 Stability of a decahedron and triangular prism NP (aspect ratios 0.15 and 0.5) of various sizes illuminated by a focused beam. Sizes of NPs are defined by the volume of a sphere with corresponding diameter. The first row shows the initial orientation of the studied objects ($\theta = 0$) and the direction of rotation. The second row shows the optical torque in the direction of axis of rotation. (a) Decahedron is stably oriented in parallel with the polarization direction (see the inset). (b) and (c) Smaller triangular prisms are oriented with their base in parallel with the field polarization while base of the larger ones are oriented perpendicularly.

We demonstrate experimentally and support theoretically three-dimensional confinement of large gold nanoparticles in an optical trap based both on very low and high numerical aperture optics. The key feature enabling stable optical trapping of larger gold NPs of certain shapes is their orientation with respect to the trapping beam polarization. Our calculations showed, that especially flat NPs tend to orient perpendicularly to the polarization of trapping beam, see figure 2. This decreases light scattering by such objects as well as the force of radiation pressure and allows stable particle trapping. Further, we demonstrated theoretically that unique properties of gold NPs allow an increase of trapping force by an order of magnitude at certain aspect ratios.

These results pave the way to spatial manipulation of plasmonic nanoparticles using an optical fiber, with interesting applications in biology and medicine.

This work was supported by the Grant Agency of the Czech Republic (project GB14-36681G)

References:

- [1] Hansen P. M., Bhatia V. K., Harrit N., Oddershede L., *Nano Lett.* **5** (2005), p. 1937–1942
- [2] Brzobohaty O., Siler M., Trojek J., Chvatal L., Karasek V., Patak A., Pokorna Z., Mika F., Zemanek P., *Scientific Reports* **5** (2015), p. 8106
- [3] Brzobohaty O., Siler M., Trojek J., Chvatal L., Karasek V., Zemanek P., *Optics Express* **23** (2015), p. 8179-8189

PRINCIPAL COMPONENT ANALYSIS OF RAMAN SPECTROSCOPY DATA FOR DETERMINATION OF BIOFILM FORMING BACTERIA AND YEASTS

M. Siler^{1*}, O. Samek¹, S. Bernatova¹, K. Mlynarikova², J. Jezek¹, M. Sery¹, V. Krzyzaneck¹, K. Hrubanova¹, V. Hola², F. Růžička², P. Zemánek¹

¹Institute of Scientific Instruments of the CAS, v.v.i., Kralovopolska 147, 61264 Brno, Czech Republic

²Masaryk University and St. Anne's Faculty Hospital, Department of Microbiology, Faculty of Medicine, Pekarska 53, 656 91 Brno, Czech Republic

*e-mail: siler@isibrno.cz

Many microorganisms (e.g., bacteria, yeast, and algae) are known to form a multi-layered structure composed of cells and extracellular matrix on various types of surfaces. Such a formation is known as the biofilm. Special attention is now paid to bacterial biofilms that are formed on the surface of medical implants, surgical fixations, and artificial tissue/vascular replacements. Cells contained within such a biofilm are well protected against antibiotics and phagocytosis and, thus, effectively resist antimicrobial attack.

A method for in vitro identification of individual bacterial cells as well as yeast colonies is presented. Figure 1 shows an example of the biofilm formed by *Staphylococcus epidermidis* bacteria and *Candida parapsilosis* yeasts known for forming biofilms. The presented method is based on analysis of spectral "Raman fingerprints" obtained from the single cell or whole colony, see figure 2(top). Here, Raman spectra might be taken from the biofilm-forming cells without the influence of an extracellular matrix or directly from the bacterial/yeast colony.

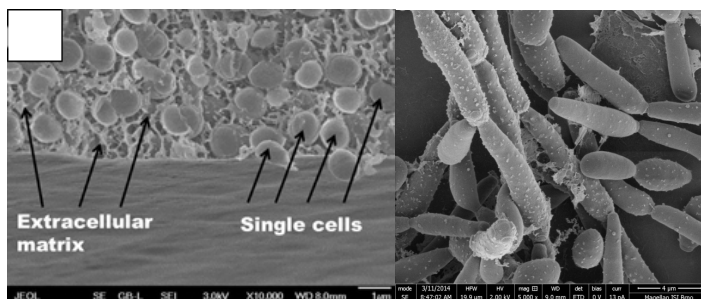


Figure 1 Scanning electron microscopy (SEM) images of *Staphylococcus epidermidis* colonies (left) and *Candida parapsilosis* yeasts (right) grown on a glass substrate. Biofilm (extracellular matrix or slime) formation is clearly visible throughout the sample filling the space between grape-like clusters of *Staphylococcus* cells. Individual cells and biofilm (extracellular matrix or slime) are denoted by arrows.

The obtained fingerprints are then transformed using singular value decomposition which serves as a foundation for the Principal Component Analysis (PCA). PCA provides an approximation of a data matrix Y in terms of the product of two smaller matrices R and L' which capture the essential data patterns of Y . The columns of R (named scores) give a picture

of the dominant object patterns of Y and, analogously, the rows of L' (loadings) show the complementary variable patterns. In the case of an spectroscopic data matrix the object will be samples measured and the variables the Raman shift or wavenumber. Figure 2(bottom) show the PCA scores plot relating the first two columns of R that describe majority of the spectral fingerprints variance. One can here clearly see the separation of scores into biofilm-positive and biofilm-negative groups. Therefore, results of principal component analyses of Raman spectra enabled us to distinguish between the two strains of *Staphylococcus epidermidis* or between two types of *Candida parapsilosis* yeasts. Thus, we propose that Raman spectroscopy can become the technique of choice for a clearer understanding of the processes involved in bacterial biofilms which constitute a highly privileged way of life for bacteria or yeasts, protected from the external environment [1,2].

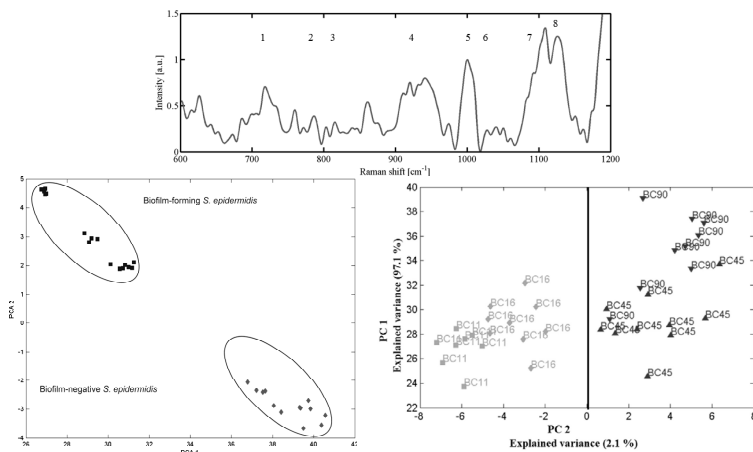


Figure 2 (top) Typical Raman spectra of *S. epidermidis* cells (biofilm-forming *S. epidermidis* CCM 7221). (bottom) Scores or values of the first two principal components PC1 and PC2 obtained from Raman spectra. (bottom-left) Scores plot for biofilm positive and biofilm negative *S. epidermidis*. (bottom-right) Scores plot for four *Candida parapsilosis* strains, biofilm positive BC 11, BC 16, and biofilm negative BC 45 and BC 90.

This work was supported by the Grant Agency of the Czech Republic (projects GA15-20645S, GA16-12477S) and by Ministry of Education Youth and Sports Czech Republic (project LO1212).

References:

- [1] Samek O., Mlynarikova K., Bernatova S., Jezek J., Krzyzanek V., Siler M., Zemanek P., Ruzicka F., Hola V., Mahelova M., Int. J. Mol. Sci. **15** (2014), p. 23924-23935
- [2] Samek O., Bernatova S., Jezek J., Siler M., Sery M., Krzyzanek V., Hrubanova K., Zemanek P., Hola V., Ruzicka F., J. Biomed. Opt. **20** (2015), 051038

TRAPPING AND COOLING OF SINGLE IONS FOR FREQUENCY METROLOGY AND QUANTUM OPTICS EXPERIMENTS

L. Slodička², T.P. Minh¹, A. Lešundák¹, V. Hucl¹, M. Čížek¹, J. Hrabina¹, Š. Řeřucha¹, J. Lazar¹, P. Obšil², R. Filip², O. Číp¹

¹Institute of Scientific Instruments of CAS, Královopolská 147, 612 64 Brno, CZ

²Department of Optics, Palacky University, 17. listopadu 1192/12, 771 46 Olomouc, CZ

Single trapped ions trapped in Paul traps correspond to ideal candidates for realization of extremely accurate optical atomic clocks and practical studies of the light–atom interactions and nonlinear mechanical dynamics. These systems benefit from both, the superb isolation of the ion from surrounding environment and excellent control of its external and internal degrees of freedom, at the same time, which makes them exquisite platforms for experimental studies and applications of light matter interaction at its most fundamental level. The exceptional degree of control of single or few ion's state enabled in past decade number of major advancements in the applications from the fields of experimental quantum information processing and frequency metrology, including recent realization of scalable Shor's algorithm^[1], fractional uncertainties of the frequency measurements close to 10^{-18} level^[2], or simulations of complex quantum many-body effects^[3]. These results, together with the rapid advancements in the production of low-noise segmented micro-traps, promise prompt access to long-desired regimes of quantum optomechanics and further development and applications of optical atomic clocks.

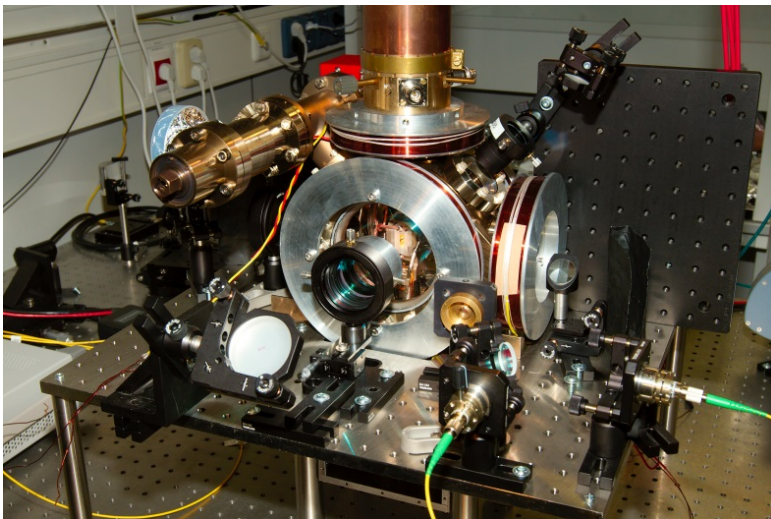


Figure 1 The view of the ion trapping and cooling apparatus in laboratories of Institute of Scientific Instruments AS CR in Brno.

We report on our recent experimental progress in the realization of single-ion trapping apparatus with the focus on metrology and quantum optomechanical experiments at Institute of Scientific Instruments in Brno together with Department of Optics at Palacky University in Olomouc, see in Figure 1. We present our experiments and infrastructure for trapping and laser-cooling of single $^{40}\text{Ca}^+$ ions including the realization of the Paul trap and its driving electronics, vacuum generation, laser locking and light detection schemes. Furthermore, we discuss two of our currently pursued efforts, detection of the nonclassical light from large number of single ion - single photon emitters^[4] and scheme for the stabilization of frequency comb parameters using the dark-resonance-spectroscopy on ion's dipole transitions^[5].



Figure 2 The snapshot of ^{40}Ca ions in the ion Coulomb crystal taken with a camera.

The research is supported by Grant Agency of the Czech Republic (project GB14-36681G), Ministry of Education, Youth and Sports of the Czech Republic (projects LO1212 and CZ.1.05/2.1.00/01.0017) and by Czech Academy of Sciences (project RVO:68081731).

References:

- [1] T. Monz, D. Nigg, E. A. Martinez, M. F. Brandl, P. Schindler, R. Rines, S. X. Wang, I. L. Chuang, Rainer Blatt, *Science* 351, pp. 1068-1070 (2016).
- [2] Ludlow A.D., Boyd M.M., Ye J., Peik E., and Schmidt P. O., *Rev. Mod. Phys.* 87, 637 (2015)
- [3] K. K. M.-S. Chang, S. Korenblit, R. Islam, E. E. Edwards, J. K. Freericks, G.-D. Lin, L.-M. Duan, C. Monroe, *Nature* 465, 590–593 (2010)
- [4] L. Lachman, L. Slodička, R. Filip, *Sci. Rep.* 6, 19760 (2016)
- [5] S. Y. Zhang, J. T. Wu, Y. L. Zhang, J. X. Leng, W. P. Yang, Z. G. Zhang, and J. Y. Zhao, *Sci Rep.* 5, 15114 (2015)

A GRAPHENE RING-CATHODE FIELD EMITTER

X. Shao, A. Srinivasan, and A. Khurshheed*

Department of Electrical and Computer Engineering, National University of Singapore, Singapore 117576

*e-mail: eleka@nus.edu.sg

The idea of using a ring-cathode source for focused electron/ion beam applications where they have several orders of magnitude greater emission area in comparison to a conventional field emission source (ring diameters in the micron range) was first proposed by Khurshheed [1]. By using direct ray trace simulations, Khurshheed predicted that the final probe size can be in the tens-of-nanometer range using first order and second order off-axis geometric aberration correction methods. With this aim in mind, tubular graphene is an ideal choice for a ring emitter as it can be produced to have a large tube diameter (typically in the micron range) while the edge thickness of the tube can be as small as a few nanometers.

In this study, initial experimental results from a graphene ring-cathode field emitter are reported, the first of its kind, which consists of a graphene tube grown in-situ on a sharp nickel wire tip (Fig. 1a). The diameter of these emitters is around 5-10 μm and the edge of the ring is approximately 4 nm in thickness (Fig. 1b). The method of producing these emitters is scalable which makes it easy to integrate it with other micromachining processes. As the graphene tube is grown directly on the wire tip, there is no need for any delicate transfer process, as was previously the case for large diameter thin tubular graphene and single strand CNT emitters. Therefore problems of alignment to the electron optical axis are eliminated.

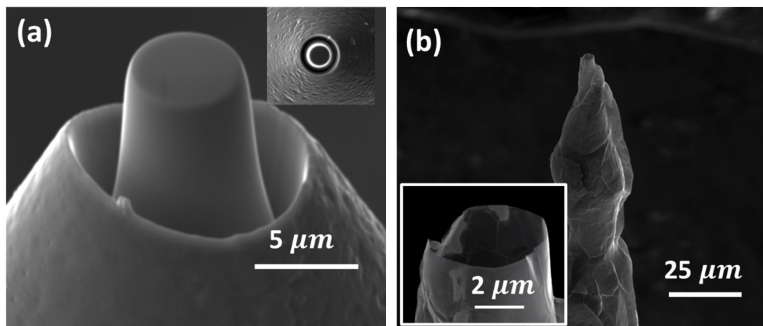


Figure 1 (a) SEM images of a concentric Ni pillar formed on top of a Ni wire tip (b) SEM image of concentric graphene ring-cathode field emitter; inset at high magnification.

A high field emission current of about 30 μA was obtained in a vacuum level of $\sim 5 \times 10^{-7}$ Torr upon application of an electric field of ~ 1.75 V/ μm (Figure 2a). This emission current is three orders of magnitude better than that reported on LaB₆ nanowire cold field emitter nanowires (~ 32 nA) [2] and a few times better than previous studies on single tip CNT emitters (< 12 μA) [3-5]. The current stability over time of the graphene ring-cathode field emitter is shown in Figure 2b [6].

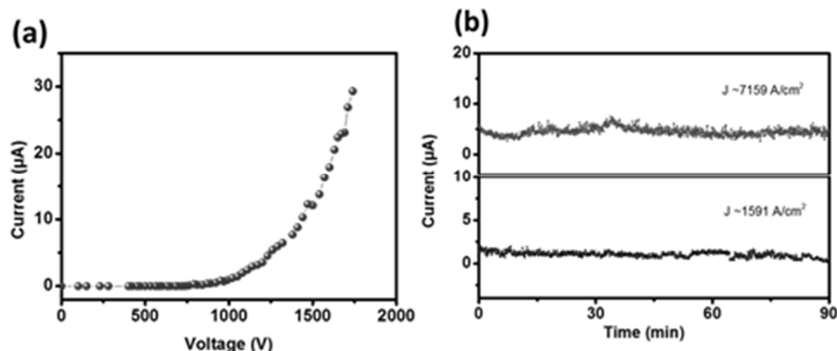


Figure 2 Field emission characteristics of the concentric graphene ring-cathode field emitter. (a) I-V curve. (b) Current stability (I-t curve) of the concentric ring-cathode graphene field emitter.

References:

- [1] A. Khurshheed, "Design of a focused electron beam column for ring-cathode sources," *Ultramicroscopy*, vol. 128, pp. 10-23, 2013.
- [2] H. Zhang, J. Tang, Q. Zhang, G. Zhao, G. Yang, J. Zhang, *et al.*, "Field emission of electrons from single LaB₆ nanowires," *Advanced Materials*, vol. 18, pp. 87-91, 2006.
- [3] N. d. Jonge, M. Allieux, M. Doytcheva, M. Kaiser, K. B. K. Teo, R. G. Lacerda, *et al.*, "Characterization of the field emission properties of individual thin carbon nanotubes," *Applied Physics Letters*, vol. 85, pp. 1607-1609, 2004.
- [4] H. Nakahara, S. Ichikawa, T. Ochiai, Y. Kusano, and Y. Saito, "Carbon nanotube electron source for field emission scanning electron microscopy," *e-Journal of Surface Science and Nanotechnology*, vol. 9, pp. 400-403, 2011.
- [5] S. K. Kanth, A. Sharma, B. C. Park, and H. S. Kim, "Multiwalled carbon nanotube field emitter as an electron source for a microcolumn," *Journal of Vacuum Science & Technology B*, vol. 34, p. 011805, 2016.
- [6] N. De Jonge, Y. Lamy, K. Schoots, and T. H. Oosterkamp, "High brightness electron beam from a multi-walled carbon nanotube," *Nature*, vol. 420, pp. 393-395, 2002.

A MICROFOCUS X-RAY TUBE WITH HIGH POWER

A. Trubitsyn, E. Grachev, M. Dubkov

Ryazan State Radio Engineering University, 390005 Ryazan, Gagarina st. 59/1
e-mail: assur@bk.ru

Microfocus X-ray tubes are means to obtain unique information on micro- and macrostructure of studied materials. Microfocus tubes allow acquiring high quality shadow images, including enlarged ones, of objects under the low radiation dose in contrast to macrofocus ones. Quality and volume of retrieved information are determined by focus sizes (X-ray radiation area on the anode) and radiation power. These two requirements are contradictory. Decrease of the focal spot sizes requires decrease of power since there is meltdown, evaporation and damage of the anode material (anticathode) due to high local heating. Standard power restriction of the fine-focused through-target source under focus diameter 100 μm on the plane anode is specified by the top power limit about 10 W.

One of the methods to increase power of X-rays without increase of the effective zone consists in formation of a narrow conical channel which walls become sources of X-rays under bombardment by high energetic electrons in the thick W anode (Fig. 1) [1].

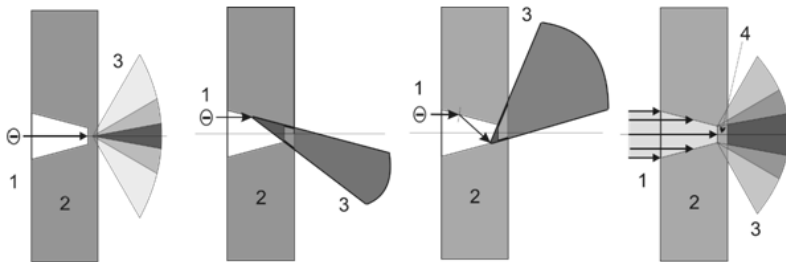


Figure 1 Generation of X-rays in the conical channel of a thick anode: 1 – an accelerated electron, 2 – an anode, 3 – X-rays, 4 – an effective area of the X-ray quantum output.

In this case emission area and consequently radiation power are significantly higher in comparison with standard plane channels, but effective area of the quantum emission (departure) is determined only by area of the channel base (a smaller base of the truncated cone) and it could be indefinitely small. This is related to the fact that X-ray spreading not in direction of the cone base is absorbed by the thick anode walls. Realization of such design allows dissipating power along the whole channel lateral surface and decreasing heat load to the target.

However, in such circuit due to reflection of electrons from channel walls, major part of the electron flow will be concentrated and absorbed in the area of the output (smaller) channel base. And basic heat loads to the anode will be also concentrated here. Absorption of electrons by conical channel walls becomes steadier in the case of electron “landing” on the lateral surface of the cone only close to input to the channel. In this case electron flow should be hollow. Fig. 2 represents an electron-optical scheme of the microfocus X-ray tube

providing focusing of the electron flow emitted by a hollow cylindrical cathode to input of the conical channel. Simulation of the tube has been carried out by the copyrighted application software "FOCUS" [2]. Calculated power of the tube is about 100 W.

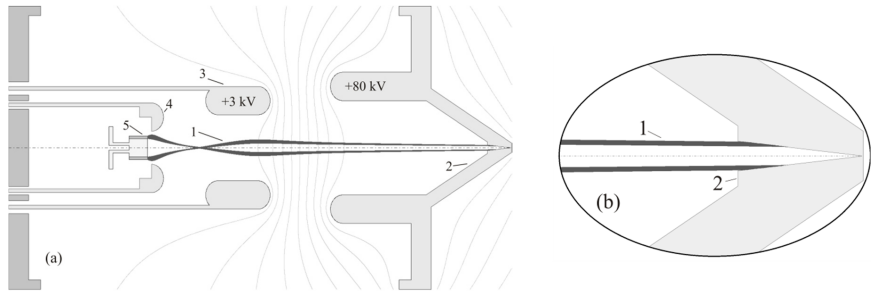


Figure 2 Microfocus X-ray tube of high power: (a) an electron-optical circuit, (b) input of electron flow 1 into the conical channel executed in the anode 2. Here 3 – a focusing electrode, 4 – a Wehnelt electrode, 5 – a hot cathode.

The research was performed by the grant of Russian Science Foundation (the project number 15-19-00132).

References:

- [1] Albert Bouwers. X-ray Tube // US Patent 1,717,309. Patented June 11, 1929.
- [2] Trubitsyn A.A. The software "FOCUS" to simulate axi-symmetrical and planar electron (ion) optical systems // Abstracts of the 8th International Conference on Charged Particle Optics (CPO-8). Software Demo Session. - Singapore, 2010.- P.208-209.

MULTIMODE FIBRES: SEEING THROUGH CHAOS

T. Tyc^{1*}, T. Čížmár² and M. Plöschner³

¹Department of Theoretical Physics and Astrophysics, Masaryk University, Kotlářská 2, 61137 Brno, Czech Republic

²School of Engineering, Physics and Mathematics, University of Dundee, Nethergate, Dundee DD1 4HN, United Kingdom

³Department of Physics, Macquarie University, Sydney, NSW 2109, Australia

*e-mail: tomtyc@physics.muni.cz

Optical fibre is a fascinating system that enables fast transport of huge amounts of information over large distances. However, so far this information has been almost always encoded into the temporal part of light propagating in the fibre by means of its amplitude or phase modulation, and the richness of the spatial degrees of freedom was mostly left unused. This was due to the rapid mixing of this spatial information during the propagation through multimode fibres: multiple chaotic-like reflections inside the fibre make it almost impossible to tell what was the light pattern at one end of the fibre when we have access to the other end only, see Fig. 1. This was also the reason why no single-fibre endoscope has been built; to transfer a spatial light information, many thousands of fibres have to be used as it is common in standard endoscopes.

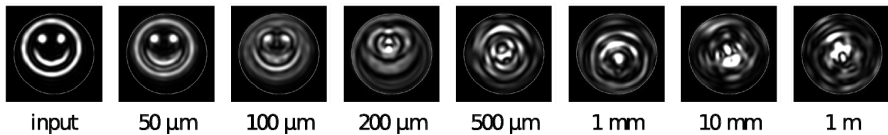


Figure 1 The light pattern at the output of a multimode optical fibre with step refractive index for different fibre lengths (shown under the images) if there is a smiley pattern at the input. The fibre has radius $12\ \mu\text{m}$ and numerical aperture 0.1, the wavelength of light is $532\ \text{nm}$. The pattern gets “mixed” quickly such that it seems to be impossible to infer the input image from the actual pattern.

On the other hand, light propagation in an optical fibre can be described very accurately by Maxwell's equations, which should in principle allow to infer the input light pattern from the output one. This can be done by employing the propagation invariant modes (PIMs, see Fig. 2) that do not change upon propagation but only gain phase. The problem is that the phases obtained by different PIMs differ by thousands of radians for fibres just a few decimeters long, and depend strongly on fibre parameters such as radius, numerical aperture etc. that need to be determined with an extremely high accuracy. Since it is very difficult to measure these parameters with the required precision directly, it is necessary to measure first the fibre transformation matrix using methods of digital holography realized by a spatial light modulator [1]. Once the transformation matrix of the fibre is known, one can use it for performing imaging by the fibre, i.e., for creating a single fibre endoscope, as well as for precise determining the fibre parameters. With the knowledge of these, one can relatively easily re-calculate the transformation matrix theoretically for different geometric shapes of the

fibre (when it is deformed) and still perform imaging, without the necessity of measuring the matrix again.

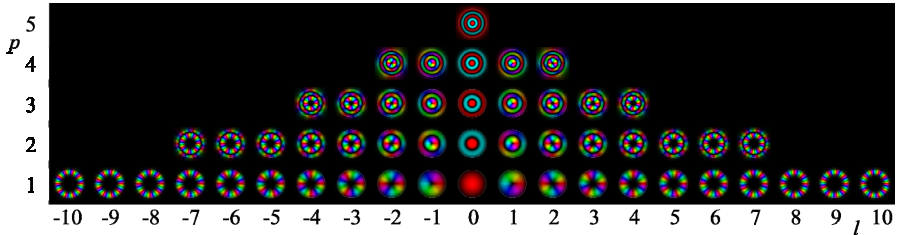


Figure 2 Propagation invariant modes of light in the fibre as in Fig. 1. The mode index l expresses the orbital angular momentum (topological charge) and the index p is related to the number of radial nodes. Light intensity and phase is expressed by colour brightness and hue, respectively.

We have realized the above described procedure in the laboratory of Dr. Tomáš Čižmár at University of Dundee [2]. It was demonstrated that our theory matches the experiment very well for commercial fibres. We were also able to identify the spin-orbit interaction and influence of fine aberrations of the refractive index from the ideal step function. This way we paved the way to completely new single-fibre endoscopes that could image microscopic objects such as neurons or other cells hidden deeply in the tissue, see Fig. 3. This could lead to new minimally invasive methods of exploring brain and other tissues and enable investigating e.g. causes of diseases such as Alzheimer's.

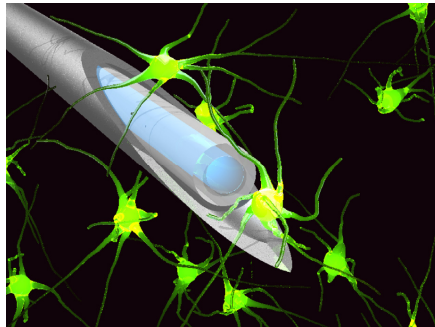


Figure 3 A microscopic endoscope inserted through an injection needle into the brain can be used to observe neurons in vivo.

References:

- [1] Čižmár, T. & Dholakia, K. *Exploiting multimode waveguides for pure fibre-based imaging*. Nature Commun. 3, 1027 (2012).
- [2] M. Plöschner, T. Tyc and T. Čižmár, *Seeing through chaos in multimode fibres*, Nature Photonics 9, 529 (2015).

ELEMENTS OF A GUIDED ELECTRON BASED QUANTUM ELECTRON MICROSCOPE: ELECTRON GUIDE, ELECTRON BEAM SPLITTER AND ELECTRON RESONATOR

R. Zimmermann¹, P. Weber¹ and P. Hommelhoff¹

¹ Department Physik

Friedrich Alexander University Erlangen-Nuremberg (FAU),

Staudtstraße 1, 91052, Erlangen, Germany

*e-mail: robert.martin.zimmermann@fau.de

We report on the manipulation of slow electrons (1...100 eV) in free space using microwave fields applied on micro-structured copper chips. The working principle of the structures is the same as for the two-dimensional Paul trap, i.e. a microwave potential applied to electrodes causes an oscillating electric field by which the electrons can be guided [1]. In order to achieve stable confinement of the electrons in a guide with our parameters, the oscillating drive frequency needs to lie in the gigahertz range. The resulting tight transverse confinement is described by a microwave pseudopotential and enables the precise control of the transverse motion of guided electrons.

By generating these fields with a planar microwave chip, an entirely new electron toolkit arises that enables guiding and steering of electrons. Furthermore, the chip-based implementation is ideally suited for the realization of an electron resonator and beam splitter.

As a key feature, this chip-based technology provides a tight transverse guiding potential and hence high transverse oscillation frequencies, which set the timescale of the transverse electron motion in the guide. In contrast to experiments employing conventional electron optics, which rely on static electromagnetic fields, the transverse confinement naturally provides discretized motional quantum states that govern the electron motion if its transverse energy is small. The goal is to employ these quantum states to demonstrate the principle of an “interaction-free measurement” [2, 3] with free electrons, which would pave the way for the development of the Quantum Electron Microscope (QEM). [4, 5]

Specifically, we discuss the design and experimental results of a planar quadrupole guide. Electrons with kinetic energies up to 10 eV are guided along a curved electrode geometry. The stability of electron guiding as a function of drive parameters and electron energy has been studied and a comparison with numerical particle tracking simulations yields good qualitative agreement. [6, 7]

Next, we detail the design and experimental demonstration of an electron beam splitter that is based on a planar microwave chip. By means of a transverse guiding potential that gradually transforms from a single well into a double well along the chip electrodes, we observe efficient beam splitting for electron kinetic energies up to 3 eV. We perform wave-optical simulations to optimize the guiding potential and to yield a smooth beam splitting without inducing an excited electron motion as adverse effect of the splitting process. In future experiments, this optimized guiding potential will provide two coherent electron beams

capable of generating interference fringes in a chip-based guided matter-wave interferometer [8].

Since theory and simulation promised better confinement than the former one-layer microwave chips, electron guides consisting of two electrode chips were designed and experimentally tested, in order to guide electron with higher kinetic energies. Guiding and splitting for electrons up to 200 eV is shown.

Lastly, mirror electrodes were added to a double-chip quadrupole in order to construct an electron resonator. By applying a periodic voltage onto the mirror electrodes and adjusting the time delay between them, the transmission of the resonator and the number of roundtrips of the electrons inside the resonator should be controlled for a given electron energy. Because one can control the time when an electron enters and leaves the guide by adjusting the voltage on the mirror electrodes, we call this a “barn door” resonator approach [5]. Preliminary results are presented.

We expect that, it should be ultimately possible to directly inject electrons into low-lying motional quantum states of the guide by mode-matching injected electron wave packets to the quantum ground state wave function of the transverse guiding potential. As prerequisites this necessitates a guiding potential that provides electrons a smooth passage into the guide and, additionally, a suitable electron gun with a well-collimated, diffraction-limited electron beam.

References:

- [1] W. Paul, *Rev. Mod. Phys.* 62, 531 (1990)
- [2] A. C. Elitzur, Lev Vaidman; *Foundations of Physics*, July 1993, Volume 23, Issue 7, pp 987-997
- [3] W. P. Putnam and M. F. Yanik; *PHYSICAL REVIEW A* **80**, 040902(R) (2009)
- [4] P. Kwiat, H. Weinfurter, T. Herzog, A. Zeilinger, and M. A. Kasevich; *Phys. Rev. Lett.* 74, 4763 (1995)
- [5] P. Kruit, R.G. Hobbs, C-S. Kim, Y. Yang, V.R. Manfrinato, J. Hammer, S. Thomas, P. Weber, B. Klopfer, C. Kohstall, T. Juffmann, M.A. Kasevich, P. Hommelhoff, K.K. Berggren; *Ultramicroscopy*, Volume 164, May 2016, Pages 31-45
- [6] J. Hoffrogge, R. Fröhlich, M. A. Kasevich and P. Hommelhoff; *Phys. Rev. Lett.* 106, 193001 (2011)
- [7] J. Hoffrogge and P. Hommelhoff; *New J. Phys.* 13, 095012 (2011)
- [8] J. Hammer, S. Thomas, P. Weber, and Peter Hommelhoff; *Phys. Rev. Lett.* 114, 254801 (2015)

